Carbohydrate Polymers 375 (2026) 124671

Contents lists available at ScienceDirect

Carbohydrate Polymers

journal homepage: www.elsevier.com/locate/carbpol

Characterisation, biocompatibility, and immunogenicity of tunicate-derived nanocellulose for tissue engineering

Matthew L. Turner [a,*], Thomas H. Jovic [a,b], Lydia S. Bullock [c], Laurence Hill [a], Bethan R. Thomas [d], Salvatore A. Gazze [e], Thierry G.G. Maffeis [f], Lewis W. Francis [e], Karl Hawkins [e], Yannick M. Sillmann [g], Ana M.P. Baggio [g], Peter R. Dunstan [c], Catherine A. Thornton [d], Fernando P.S. Guastaldi [g], Mark A. Randolph [h], Iain S. Whitaker [a,b]

[a] Reconstructive Surgery & Regenerative Medicine Research Centre, Swansea University Medical School, SA2 8PP, UK
[b] Welsh Centre for Burns & Plastic Surgery, Morriston Hospital, Swansea, SA6 6NL, UK
[c] Physics Department, College of Science, Swansea University, SA2 8PP, UK
[d] Swansea University Medical School, SA2 8PP, UK
[e] Centre for NanoHealth, Swansea University, SA2 8PP, UK
[f] College of Engineering, Swansea University, SA1 8EN, UK
[g] Division of Oral and Maxillofacial Surgery, Department of Surgery, Massachusetts General Hospital, Harvard School of Dental Medicine, Boston, MA, USA
[h] Division of Plastic and Reconstructive Surgery, Department of Surgery, Massachusetts General Hospital, Harvard Medical School, Boston, MA, USA

ARTICLE INFO

Keywords:
Nanocellulose
Bioprinting
Characterisation
Tunicate
Biocompatibility
Biomaterial

ABSTRACT

Nanocellulose has gained significant traction as a viable material for tissue engineering. We investigated 3 chemically distinct varieties of tunicate-derived nanocellulose: carboxymethylated (CTC), enzymatically pre-treated (ETC), and TEMPO-oxidised (TTC), with the objective of determining a candidate scaffold material for tissue engineering. The physicochemical properties of each variant were characterised by SEM, AFM, Raman spectroscopy, and mechanical compression. Notably, ETC had the lowest aspect ratio, smallest pore diameter, greatest optical clarity, and highest ultimate compressive strength, indicating superiority as a candidate tissue engineering scaffold. Rheological analysis revealed a significantly higher loss tangent for ETC and reduced viscosity at higher temperature, compared with CTC and TTC. ETC also demonstrated superior line width resolution both before and after calcium chloride crosslinking, indicating superior print fidelity and post-printing shape retention. All materials exhibited excellent biological compatibility by live/dead staining of embedded primary chondrocytes. NC was nonimmunogenic and did not stimulate the secretion of proinflammatory mediators when combined with whole blood. The implantation of NC-based bioink into immunocompetent mice did not evoke an adverse immunological reaction, and explanted constructs retained a stable form for 14 days. Tunicate-derived NC, particularly ETC, demonstrates excellent structural, biological, and mechanical properties with great potential for tissue engineering applications.

1. Introduction

The clinical translation of 3D bioprinting technology has the potential to yield novel and personalised treatment options for patients (Lam et al., 2023). The current gold standard approaches to reconstructing tissue defects, such as those of the ear, depend largely on the use of autologous tissue transfer to restore form and function, or the use of synthetic materials or prosthetics, which lack the properties of native tissue. 3D bioprinting has the potential to obviate the need for tissue transplantation and to restore form and function without destructive, painful, or disfiguring donor sites (Uppal et al., 2008). Bioprinting additionally confers the advantage of spatial resolution and control: the anisotropy of biological tissues can be emulated at the macro- to nano-scale in order to optimise extracellular matrix (ECM) composition, cellular interactions, and topography (Wang et al., 2022).

A major challenge in bioprinting research, in particular where clinical translation is the end goal, is the pursuit of appropriate, biocompatible materials to serve as bioinks (Benwood et al., 2021). Although

* Corresponding author.
E-mail address: matthew.turner@swansea.ac.uk (M.L. Turner).

https://doi.org/10.1016/j.carbpol.2025.124671
Received 7 August 2025; Received in revised form 31 October 2025; Accepted 6 November 2025
Available online 8 November 2025

the desired properties for biomedical applications may vary between materials, the fundamental outcome of *in vivo* implementation remains universal: the regeneration of damaged tissue through repair and restoration, whilst eliminating the need for organ transplantation (Rahmani et al., 2022). Tissue-engineered scaffolds provide a temporary supporting platform for the growth of embedded cells that interface with host tissue and must intrinsically be biocompatible, non-toxic, and of appropriate mechanical strength to emulate natural tissue macro and microarchitecture (Drury & Mooney, 2003; Gungor-Ozkerim et al., 2018). The incorporation of biopolymers such as cellulose into medical devices and materials is a major focus of research in the biomedical field and has recently expanded into the 3D bioprinting domain (Jessop et al., 2019; Jovic et al., 2019; Martínez Ávila et al., 2016). Indeed, cellulose is an appealing renewable resource for use in biomedical applications where structural stability, low toxicity, and biocompatibility are paramount (Coelho et al., 2018). This makes it an ideal candidate for the development of novel functional materials with bespoke mechanical, physical, and biochemical properties (Abitbol et al., 2016).

Nanocellulose (NC) used for bioprinting is most commonly "pulp-derived", where the material is extracted from lignocellulosic biomass such as wood and agricultural residues. The microarchitecture of pulp-derived NC lends itself to cartilage tissue engineering, with biomimicry conveyed through the fibrillar structure of cellulose, along with its inherent bioactivity and biocompatibility, with recent studies highlighting a role of NC as a chondrogenic bioink (Al-Sabah et al., 2019; Jessop et al., 2019; Jovic et al., 2023; Nguyen et al., 2017).

The caveats of pulp-derived NC include potential contamination by hemicellulose, pectin, and lignin, which compromise material purity, disrupt structural and mechanical properties, and ultimately jeopardise translational potential (Rojo et al., 2015; Sugiarto et al., 2022; Yu et al., 2022). Alternative sources of NC include bacterial-derived, and, more recently, tunicate-derived NC. Tunicates provide an appealing alternative source of NC that is pure, sustainable, and affordable (Zhao & Li, 2014). Tunicates are members of the phylum Chordata, subphylum Tunicata, and are the only animals that can produce cellulose (Inoue et al., 2019) which can be harvested at scale, enabling a renewable resource of pure cellulosic material with high crystallinity (Dunlop et al., 2018). The hydroxy groups along the polymer chain serve as anchor points for the addition of functional groups such as aldehydes, carboxylic acids, amines, and macromolecules, allowing for a diverse range of modifications for multiple applications including 3D bioprinting (Lin et al., 2023; Thakur et al., 2021). By the same token, such functionalisation has the potential not only to improve the physicochemical properties of NC and its composites, but can also act as a foundation to enhance its bioactivity (Sun et al., 2022).

In this study, we characterise the biocompatibility, immunogenicity, physicochemical, and mechanical properties of enzymatically pre-treated (ETC), carboxymethylated (CTC), and TEMPO-oxidised (TTC) NC variants isolated from the marine tunicate, *Ciona intestinalis*. We hypothesise that tunicate-derived NC materials will demonstrate structural and biological suitability as a major constituent of hydrogels used for 3D-bioprinting cartilage tissue.

2. Materials and methods

2.1. Nanocellulose

Nanocellulose used in this study was purchased from Ocean TuniCell AS, Blomsterdalen, Norway, and was derived from a sustainable marine source of tunicates (*Ciona intestinalis*). The material was supplied as a 2.5% dispersion in pyrogen-free water with ≤0.5 EU/ml, < 10 CFU/ml, with a purity >99% and free of contaminating hemicelluloses and lignin. The crystallinity of the material as determined by X-ray diffraction ranged from 86.83 ± 0.66% to 89.07 ± 1.60%. Three types of NC were characterised: CTC in which hydroxy (OH) groups of the cellulose have been substituted with carboxymethyl groups (CH_2COOH; 660.8 ± 2.6 μmol/g cellulose; DS 11.3 ± 0.1%); ETC which has undergone enzymatic hydrolysis using Novozym 476; and TTC in which OH groups are substituted with carboxyl groups (COOH; 783 ± 41 μmol/g cellulose). The density of each material was 1.008 g/cm^3. The zeta potential of CTC, ETC, and TTC was -2.9 ~ -34.8 mV, -7.48 ~ -16.9 mV, and -40.3 ~ -57.2 mV, and the onset of decomposition by thermogravimetric analysis was 296 °C, 325 °C, and 268 °C, respectively.

2.2. Cryo-scanning electron microscopy (cryo-SEM)

Cryo-SEM was conducted using a Hitachi S4800 field emission scanning electron microscope (Tokyo, Japan) equipped with a Quorum PPT2000 cryogenic stage. NC samples were spread on a copper block sample holder and coated with platinum (ca. 5 nm) prior to transfer to the SEM chamber. Imaging was performed at −120 °C. Fibre dimensions and pore geometry were determined using ImageJ software V1.53k.

2.3. Atomic force microscopy (AFM)

NC was loaded onto polylysine coated mica sheets (Merck Life Science UK Ltd., Gillingham, UK). Slides were scanned in air using Peak Force Tapping mode at a scan speed of 1 Hz on a Bruker Bioscope Catalyst (Bruker Instruments, California, USA). Images were processed using first-order flattening, and dimensions were calculated from at least 50 measurements from 5 to 10 representative micrographs of each sample using Nanoscope Analysis software (V1.50) and ImageJ software.

2.4. Swelling, porosity, and water absorption

Nanocellulose/alginate (NC/alg) hydrogels were prepared by combining NC with 5% *w/v* sodium alginate (Merck Life Science; Mw 495 KDa, M/G ratio 1.9 (Gorroñogoitia et al., 2022), viscosity [2% at 25 °C] ≥ 2000 cps) which was reconstituted with phosphate-buffered saline (PBS; Life Technologies Ltd, Paisley, UK). The final formulation contained 2% NC and 1% alginate in an 80:20 *v/v* ratio, respectively (Markstedt et al., 2015). Materials were mixed using luer-lock syringes connected together, whilst avoiding the introduction of air bubbles. Pellets were dispensed from a 1 ml syringe (BD Biosciences, Oxford, UK) in 100 μl volumes and crosslinked with 100 mM calcium chloride (Merck Life Science) for 15 min at room temperature. Pellets were then immersed in PBS for 24 h at 37 °C. Excess PBS was blotted away and each pellet was weighed (M_w). Pellets were then dried in a vacuum chamber for 24 h and reweighed (M_d). PBS density was considered as 1.006 g/ml (Brown et al., 2011). The following equations were used to calculate swelling (1), porosity (2) (Al-Sabah et al., 2019), and water absorption (3) (Liu et al., 2018):

$$Swelling\ (\%) = \frac{M_w - M_d}{M_d} \times 100 \quad (1)$$

$$Porosity\ (\%) = \frac{M_w - M_d}{\rho \times V} \times 100 \quad (2)$$

where ρ is PBS density and V is pellet volume.

$$Water\ absorption\ (\%) = \frac{M_w - M_d}{M_w} \times 100 \quad (3)$$

2.5. Raman spectroscopy

Raman spectra were obtained using an inVia Inspect Raman spectrometer (Renishaw, Gloucestershire, UK). Approximately 10 μl of NC was pipetted onto an aluminium foil substrate and a 20× N Plan EPI objective (Leica, Colorado, USA) was used to take point spectra across the droplet. The spectra centred on 940 cm^{-1} (wavenumber range 310.53 cm^{-1} - 1483.67 cm^{-1}), 100% laser power, 5-s exposure time, 3

acquisitions of 30 accumulations each, at 5 different locations in the sample.

2.6. Rheology

The rheological properties of NC were measured using an AR-G2 Controlled Stress Rheometer (TA instruments, Cheshire, UK) fitted with a 40 mm diameter parallel plate geometry. Approximately 1 ml of sample was loaded onto the centre of the lower plate of the rheometer, and the upper plate was gradually lowered onto the sample until the gap was filled (gap = 500 μm). The normal force measured at the lower plate was set at a maximum of 0.1 N. To evaluate the effect of temperature on each sample, the lower temperature-controlled Peltier plate was set to 10 °C, 25 °C, or 37 °C.

Following a sample equilibration period of 5 min, a frequency sweep (0.1–10 Hz) was performed at a constant stress of 0.1 Pa, which was selected from within the linear viscoelastic region for each NC, as determined by amplitude-sweep (Supplementary Fig. 1-3). Each measurement was within the linear viscoelastic range of the sample as confirmed by the absence of a third harmonic in the strain response waveform. Values of storage modulus (G') and loss modulus (G") were recorded over the entire frequency range. At the end of the frequency sweep, a shear flow ramp was carried out on the same sample at logarithmically increasing shear rates in the range of 0.1–100 s^{-1} over a period of 2 min. These experiments were repeated 5 times for each sample.

2.7. Printability assessment

Print characteristics of NC/alg hydrogels were assessed using a BIO X 3D bioprinter (CELLINK, Gothenburg, Sweden). The minimum extrusion pressure was determined by increasing the pneumatic pressure of the internal pump (0–200 kPa) until the hydrogel was extruded from the printhead as a continuous filament through a 22G nozzle. The integrated bioprinter software (Heart OSTM) was used to create instructions for printing in the form of gcode files. A 30 mm line was extruded at 20 mm/s, 25 kPa, and examined by light microscopy. Line width was measured using Olympus CellSens V2.3 (Evident, Tokyo, Japan) before and after crosslinking with 100 mM $CaCl_2$ (Merck Life Science).

2.8. Mechanical compression

The static compressive strength of NC constructs was determined using a 1ST compression tester (Tinius Olsen, Pennsylvania, USA). Constructs were prepared as described in section 2.4 and cast into cylinders of 8 mm × 10 mm. They were crosslinked with $CaCl_2$ for 16 h to ensure maximum crosslinking. Cylinders were added to the base plate of the compressor, standing upright, and the upper plate was lowered to within 1 mm of the material. Upon achieving a contact pressure of 0.01 N, compression was initiated at a rate of 4 mm/min, and the material was compressed until failure.

2.9. Spectral absorbance

The optical clarity of NC was evaluated by spectral absorbance measurements using a FLUOstar Omega microplate reader (BMG Labtech, Ortenberg, Germany). Approximately 200 μl of NC was loaded into triplicate wells of UV-transparent microplates (655090; Greiner Bio-One LTD, Gloucestershire, UK) and absorbance measurements were taken between 350 nm and 750 nm at 10 nm intervals. An equivalent volume of 1% *w/v* alginate in DI water was used as a reference.

2.10. Cell isolation and culture

Nasoseptal chondrocytes were isolated from waste surgical tissue obtained from healthy donors undergoing septorhinoplasty at Singleton and Morriston Hospitals, Swansea, UK. Samples were collected after obtaining informed consent, with approval from Swansea Bay University Health Board. Ethical approval was granted by the Research Ethics Committee, National Institute for Social Care and Health Research, Welsh Government (IRAS ID 99202). Briefly, nasoseptal tissue was cut into 1 mm^3 pieces and sequentially digested with 0.2% (*w/v*) pronase for 40 min, followed by 0.24% (*w/v*) collagenase (Merck Life Science) for 16 h. Cells were cultured in DMEM supplemented with 10% foetal bovine serum, 1% penicillin-streptomycin, 1 mM D-glucose, and 0.1% non-essential amino acids (all from Life Technologies Ltd) in a humidified incubator at 37 °C with 5% CO_2. Media was replaced every 48 h and cells were grown to 80% confluence before being passaged with 0.05% trypsin-EDTA (Life Technologies Ltd). Cells were counted using a haemocytometer after staining with trypan blue for exclusion (Life Technologies Ltd). Cells were cultured up to passage 3 and used to assess viability in NC/alg hydrogels.

2.11. Cell viability

Chondrocytes were incorporated into NC/alg hydrogels (prepared as described in 2.4) at a final concentration of 3×10^6 cells/ml. Cell-laden hydrogels were dispensed as 100 μl pellets using a syringe and then crosslinked with $CaCl_2$ for 15 min. Pellets were cultured for up to 21 days, and cell viability was determined at 24 h, 4 days, 7 days, 14 days, and 21 days using LIVE/DEAD® Viability/Cytotoxicity Kit (Life Technologies Ltd) according to the manufacturer's instructions. Pellets were imaged using an Olympus IX51 inverted fluorescence microscope (Evident) and cellSens Dimension software. Percent cell viability was determined by the ratio of live (green) to dead (red) cells for each material.

2.12. Ex vivo whole blood stimulation

The immunogenicity of NC was evaluated using human whole blood, which was collected after obtaining informed consent, with approval by Swansea University Research Ethics Committee (2022–0029). Cell culture was performed aseptically using endotoxin-free materials. Blood was collected from healthy donors in a lithium heparin BD Vacutainer™ (Fisher Scientific, Loughborough, UK) and diluted 1:4 with RPMI 1640 (61870; Life Technologies) containing 1, 10, 100, or 1000 μg/ml CTC, ETC, TTC, or an equivalent volume of water as vehicle control. Lipopolysaccharide (LPS, 1 ng/ml; ultrapure LPS from *Escherichia coli* serotype 0111: B4, InvivoGen, Toulouse, France) was used as a positive control. Blood was then incubated for 4 h or 24 h in a humidified incubator at 37 °C with 5% CO_2. At the end of the experiment, blood was centrifuged at 500 *g* for 5 min to pellet red blood cells, and cell-free supernatants were collected and stored at −20 °C until use in enzyme-linked immunosorbent assay (ELISA). Acellular constructs were prepared as described in 2.14.

2.13. Animals and ethical approval

Five female immunocompetent C57BL/6 mice (8 weeks old, weighing 20–25 g) were purchased from Charles River Laboratories (Cambridge, MA, USA). Mice were housed in standard cages ($n = 5$ animals/cage) under specific pathogen-free conditions with controlled temperature (22 ± 2 °C) and humidity (55 ± 10%). All cages were equipped with nesting materials and shelters to provide environmental enrichment. All animals received ad libitum access to food and water and were maintained on a 12-h light/dark cycle. The protocol was approved by the Massachusetts General Hospital Institutional Animal Care and Use Committee, in compliance with the NIH guidelines for the care and use of laboratory animals. Only female mice were used in this study to minimise variability resulting from sex-based hormonal differences. The experiments were conducted in adherence with the ARRIVE guidelines for transparent animal research (Percie du Sert et al., 2020).

After 2 weeks, all animals were euthanised under deep surgical anaesthesia through exsanguination via cardiac puncture using a 20G needle inserted into the left ventricle, and blood samples were collected from all animals. Following blood withdrawal, cervical dislocation was performed to ensure death, in accordance with the American Veterinary Medical Association Guidelines for the Euthanasia of Animals. The explants were then harvested, inspected for structural integrity and vascularisation, and fixed for sectioning and haematoxylin and eosin (H&E) staining. The heart, liver, and kidneys were harvested and examined for any signs of systemic inflammation or toxicity.

The levels of inflammatory markers, including GM-CSF, IFN-γ, IL-1β, IL-2, IL-4, IL-10, IL-12p70, MCP-1, and TNF-α, were measured. These cytokines were assessed to evaluate the systemic inflammatory response and potential signs of toxicity associated with the implanted scaffolds.

2.14. Animal surgery

Surgeries were performed under sterile conditions by one surgeon (Y. S.) to ensure consistency. Animals were sedated with isoflurane (3–5%) via a facemask. The dorsal area was shaved, and the surgical area was disinfected with Povidone-iodine solution (Betadine®, Stamford, CT, USA). A single dose of Carprofen (5 mg/kg; subcutaneous; Rimadyl®, Kalamazoo, MI, USA) and a single dose of Buprenorphine (0.1 mg/kg; subcutaneous; Buprenorphine Hydrochloride Injection, Chestnut Ridge, NY, USA) were administered to each animal before surgery. A 1 cm midline incision was made through the skin on the animal's dorsum, and two lateral subcutaneous pockets were created by blunt dissection. Two identical constructs (each 10 mm × 10 mm × 3 mm) were placed into individual subcutaneous pockets (left and right sides). Acellular bioink constructs were prepared as described in Section 2.4 using sterile alginate (PRONOVA SLG 100; DuPont Nutrition Norge AS, Sandvika, Norway) with the addition of sterile high-molecular-weight sodium hyaluronate (0.6% final; Lifecore Biomedical, Chaska, USA) and then crosslinked. Pellets were washed 3 times in PBS before implantation. The wound was closed with 3–4 surgical staples. The incision site was injected with Bupivacaine (5 mg/ml; subcutaneous; Hospira, Lake Forest, IL, USA).

2.15. Histological analysis

The harvested tissues were fixed in a 10% formalin solution for 2 days, embedded in paraffin wax, and then sectioned at a thickness of 5 μm. The sections were mounted on glass slides, deparaffinised, and stained with H&E to evaluate the morphological and early inflammatory responses around the implanted scaffolds. The whole slides were then scanned and imaged by NanoZoomer 2.0HT Digital Pathology (Hamamatsu Photonics K.K., Japan) and analysed using NDP.View2 software (Hamamatsu).

2.16. Multiplex analysis

Mouse blood was analysed for inflammatory markers GM-CSF, IFN-γ, IL-1β, IL-2, IL-4, IL-10, IL-12p70, MCP-1, and TNF-α, using a Mouse Cytokine Proinflammatory Focused Array (Eve Technologies Corporation, AB, Canada), according to the manufacturer's instructions. Immuno-complexes were read on a FLEXMAP3D (Diasorin S.p.A., Saluggia, Italy).

Briefly, serum samples were incubated with antibody-coated microspheres, followed by the addition of a biotinylated detection antibody. Detection of the proteins was accomplished by incubation with phycoerythrin-labelled streptavidin. The resultant bead immuno-complexes were then read on a FLEXMAP3D with the instrument settings recommended by the manufacturer.

2.17. Statistical analysis

Data are reported as arithmetic mean ± standard deviation (mean ± SD). Statistical analysis was performed using SPSS version 28.0 (IBM, Armonk, NY, USA). Data were tested for normality, and comparisons between groups were made using ANOVA followed by Bonferroni *post-hoc* test. Significance was attributed when $p < 0.05$.

3. Results and discussion

3.1. Morphological properties

3.1.1. Nanofibre morphology and size

The morphology and size of NC fibres were determined from cryo-SEM (Fig. 1) and AFM images (Fig. 2), respectively. The raw material's microstructure was clearly observed through cryo-SEM micrographs. Each of the materials had similar, but distinct, microarchitecture and physical features. The NC fibrils of each sample were long and thin with varied degrees of entanglement. Some fibrils had multiple interconnections with neighbouring strands, whilst others existed as individual strands. Each type of NC consisted of a densely packed and intricate network of fibrils that often merged into broader agglomerates. Interestingly, to some degree, all samples had a 'skin-like' morphology or floc, where NC appeared to agglomerate into a homogenous layer. This feature was primarily observed at the sample surface for CTC (Fig. 1A, B) and TTC (Fig. 1E, F) but was a predominant characteristic for ETC, with flocculation apparent throughout the sample (Fig. 1C, D). Within this layer, individual fibrils were indistinguishable and appeared as a homogenous mass. This phenomenon might be a cryo-SEM artefact, or possibly the result of nanofibril rearrangement in which parallel fibrils interact through hydrogen bonding to form ordered structures typically associated with dehydrated NC (Kwak et al., 2019; Marchessault et al., 1959). However, fibrils are known to form flocs, particularly for native NC suspensions, which are polydisperse (Martoïa et al., 2015).

Fibril length measurements were challenging to perform using cryo-SEM images, as almost all fibrils were interconnected and formed large entanglements, making it difficult to distinguish the beginning and end of individual fibrils. Furthermore, fibrils processed for cryo-SEM were coated with ~5 nm platinum, which increased fibril diameter, making width measurements less accurate. Consequently, AFM was considered the most appropriate method for measuring fibril dimensions as individual fibrils were discernible following dilution of the raw material. Nanoscale objects appear wider under the AFM due to the finite dimensions of the cantilever tip, known as the "tip convolution effect" (Markiewicz & Goh, 1994). Conversely, height measurement is not influenced by the tip dimension as only the tip apex interacts with the object (Abu-Lail and Camesano, 2003). The widths of nanofibres as determined by AFM height (Fig. 2) were similar for CTC, ETC, and TTC, with a mean of 4.04 ± 0.91 nm, 5.24 ± 0.73 nm, and 4.00 ± 0.71 nm, respectively (Table 1) with an assumed cylindrical profile. The mean length of fibres was 1779 ± 940 nm, 1959 ± 960 nm, and 1899 ± 826 for CTC, ETC, and TTC, resulting in an aspect ratio of 440 ± 233, 374 ± 183, and 474 ± 206, respectively. The dimensions are consistent with previously reported values of tunicate-derived NC fibrils between 5 and 30 nm wide and 0.1 μm to >2 μm in length (Elazzouzi-Hafraoui et al., 2008; Habibi et al., 2006).

Cryo-SEM and AFM images clearly demonstrated the dimensional characteristics of each NC material. Tunicate-derived NC fibrils are generally longer than those extracted from wood and other sources and have a high crystallinity, existing almost exclusively as cellulose Iβ allomorph. Whereas, bacterial and wood-derived NC exist as Iα, with the latter often having a disordered molecular structure and as little as 30% crystallinity (Sacui et al., 2014). Tunicate-derived NC has a broad spectrum of applications, particularly in bioengineering and polymer reinforced materials, where its high aspect ratio results in greater rigidity and mechanical strength (Wang, Yu, et al., 2018). Indeed, studies

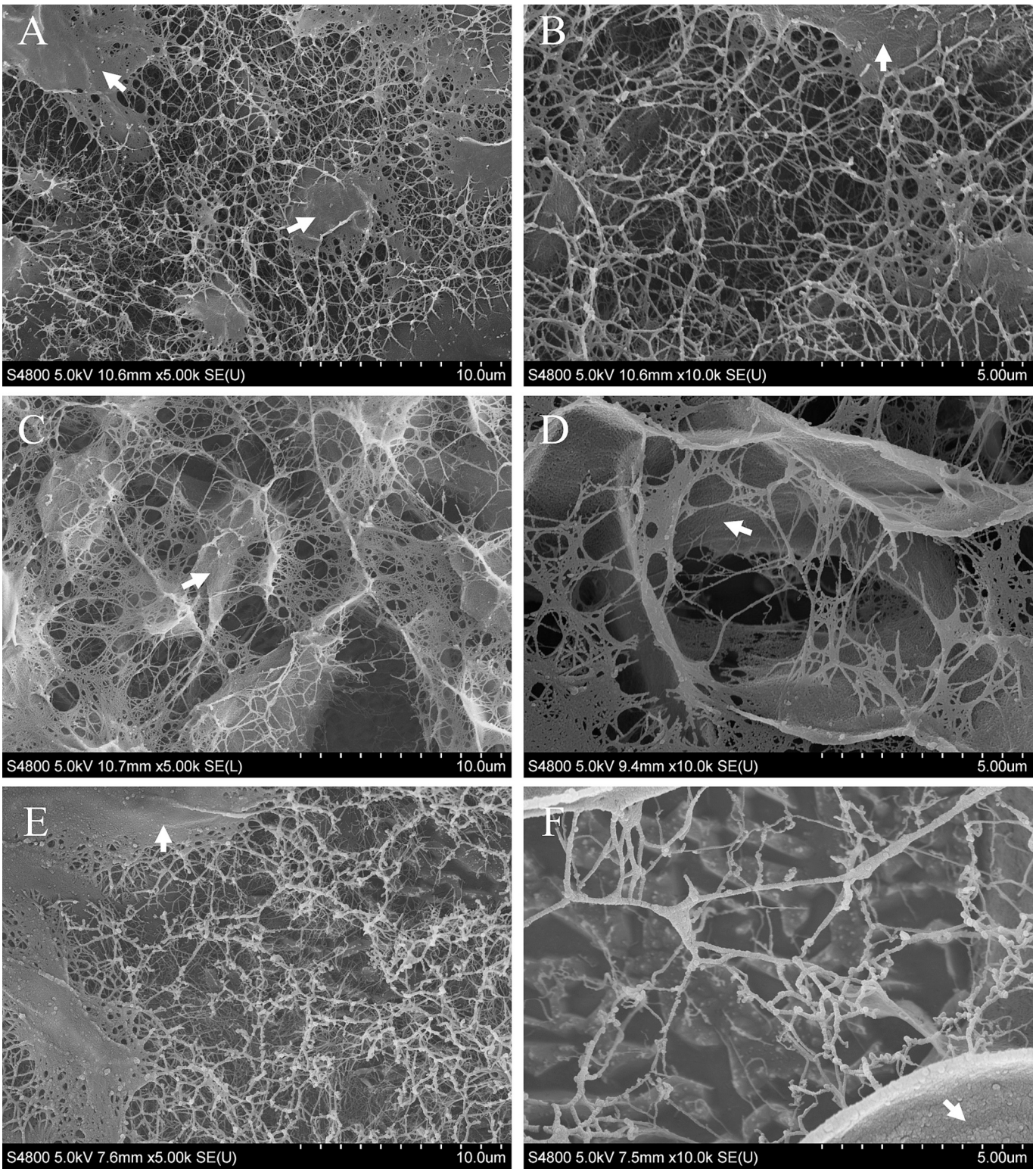

Fig. 1. Cryo-SEM micrographs of CTC (A, B), ETC (C, D), and TTC (E, F) at x 5k (left panel) and x 10k (right panel) magnification. Arrowheads indicate NC sheets within the material. Representative images are shown.

of the mechanical properties of polymer nanocomposites made by combining low and high aspect ratio NC (cotton and tunicate, respectively) are firmly aligned with the mechanical properties of the high aspect ratio material, even when combined in a 1:1 ratio (Sapkota et al., 2017). Consequently, NC hydrogels can be formulated as bioinks with lower aspect ratio materials, which are often cheaper and have different physicochemical properties, without compromising the structural integrity of the nanocomposite as a whole.

3.1.2. *Porosity*

Each of the NC materials had an extensive porous microarchitecture consisting of highly interconnected and tortuous fibrillar networks with

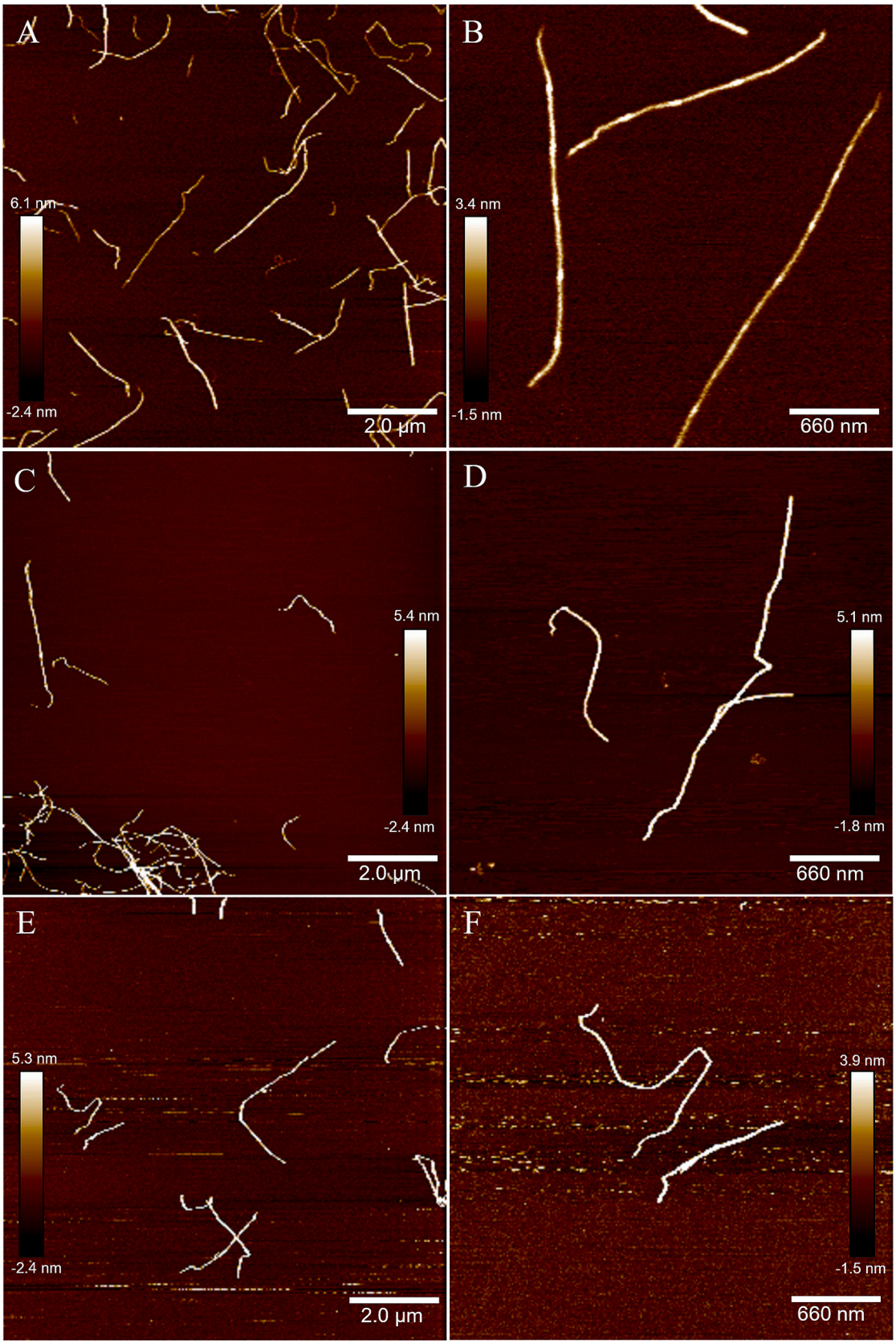

Fig. 2. AFM analysis of CTC (A, B), ETC (C, D), and TTC (E, F) at low (left panel) and high (right panel) resolution. Representative images from 3 independent experiments.

Table 1
Dimensions of CTC, ETC, and TTC fibrils determined from AFM images. Mean and aspect ratio ± SD from at least 20 independent measurements.

	CTC		ETC		TTC	
	Width (nm)	Length (nm)	Width (nm)	Length (nm)	Width (nm)	Length (nm)
Mean	4.04 ± 0.91	1779 ± 940	5.24 ± 0.73	1959 ± 960	4.00 ± 0.71	1899 ± 826
Median	4.29	1780	5.01	1612	3.76	2269
Min	2.44	323	4.47	566	2.95	264
Max	5.13	4241	6.70	3544	5.89	3677
Aspect ratio	440 ± 233		374 ± 183		474 ± 206	

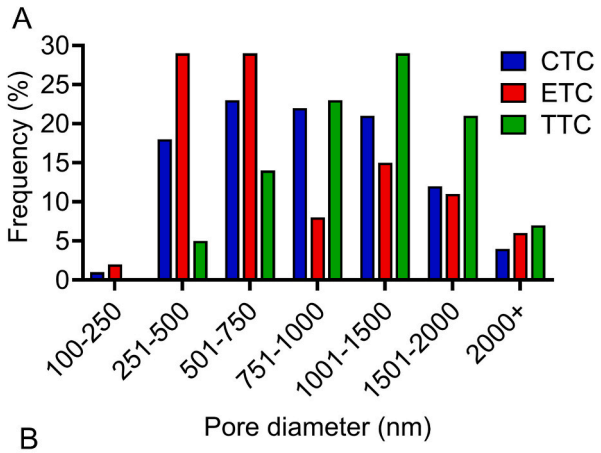

B

	Pore diameter (nm)			
	Mean	Minimum	Maximum	Median
CTC	974 ± 575	244	3,530	838
ETC	887 ± 599	191	2,970	667
TTC	1,279 ± 685	375	3,808	1,185

Fig. 3. Pore diameter size distribution (A) and mean, minimum, maximum, and median pore diameters (B) of CTC, ETC, and TTC, taken from at least 50 independent measurements.

varying degrees of entanglement and void spaces (Fig. 1). The mean pore diameters of CTC, ETC, and TTC were 974 ± 575 nm, 887 ± 599 nm, and 1279 ± 685 nm, respectively. Despite comparable fibril diameters in this study, the distribution of pore sizes differed between groups (Fig. 3A). Fibril diameter is known to influence pore size. Studies of porous nanofibrous assemblies have described the counter-intuitive finding that a reduction of fibril diameter does not increase the mean pore radius but instead results in smaller pores, whilst the inverse is also true (Eichhorn & Sampson, 2005; Nelson et al., 2012).

Approximately 65% of CTC pore diameters were between 501 and 1500 nm in width, and 19% of pores had diameters up to 500 nm, with just 1% within the 100–250 nm range. The remaining 16% of pore diameters were over 1500 nm in length, with 4% being above 2000 nm. For ETC, 52% of pore diameters were in the range of 501–1500 nm, with 31% in the range of 100–500 nm. Similar to CTC, the percentage of pore diameters above 1500 nm was 17%, with 6% exceeding 2000 nm. Finally, for TTC 66% of pore diameters were in the range of 751–1500 nm, with just 5% below 500 nm and none under 250 nm. Of the three types of NC, TTC had the greatest proportion of larger pores, with 29% above 1500 nm and 7% > 2000 nm. Whilst ETC had the greatest proportion of smaller pores. The mean, minimum, maximum, and median pore diameters are listed in Fig. 3B.

The porosity, swelling, and water absorption of NC/alg hydrogels were determined primarily by the relative differences in material weight when fully hydrated and fully dehydrated. There was no significant difference between the porosity of CTC/alg and ETC/alg hydrogels (37.5 ± 3.8% vs 40.0 ± 2.6%, respectively), nor between ETC/alg and TTC/alg hydrogels (41.7 ± 1.4%; Fig. 4B). However, there was a significant difference between the porosity of CTC/alg and TTC/alg ($p = 0.05$) with TTC having a higher percent porosity. As expected, the porosity of the NC/alg hydrogels was significantly lower than that of alginate alone (64.1 ± 7.2%, $p < 0.05$ for all).

Pore diameter (Fig. 4A) may be influenced by the distinct chemical modifications present on each material, which influence the repulsion and attraction of individual fibrils. Interestingly, the increased porosity of TTC/alg aligns with the mean pore diameter of TTC, as observed by cryo-SEM. TTC had a significantly larger mean pore diameter than CTC or ETC (1279 ± 685 vs 974 ± 575, $p < 0.01$; and 887 ± 599, $p < 0.001$, respectively), however, there was no significant difference between the mean pore size of CTC and ETC. Porosity and pore geometry are important determinants of cellular migration and behaviour, with smaller pore sizes (<100 nm) facilitating extracellular matrix deposition and larger pores (100 nm to 100 μm) promoting cell migration, proliferation, and neovascularisation (Mukasheva et al., 2024). Of note, recent studies of tunicate-derived NC have demonstrated construct neovascularisation *in vivo*, highlighting the advantageous nature of pore geometry in this range for facilitating vascular ingress: a key attribute for translational tissue engineering (Apelgren et al., 2021).

The hydrophilic nature of NC, coupled with surface modifications such as carboxymethylation and carboxylation, which are known to decrease zeta potential, may impact the interaction of the material with water molecules and, thus, influence swelling. Each NC/alg hydrogel exhibited comparable swelling characteristics with no significant difference between groups (CTC/alg 1527.4 ± 102.2%, ETC/alg 1590.1 ± 67.4%, and TTC/alg 1620.8 ± 30.0%, Fig. 4C). However, there was a trend towards significance between CTC/alg and TTC/alg ($p = 0.069$), with TTC/alg having increased swelling capacity. The swelling capacity of alginate alone was significantly higher than all NC/alg hydrogels (4036.2 ± 363.4%, $p < 0.05$), Fig. 4C). As expected, the water absorption behaviour of hydrogel materials was similar to the swelling properties. For NC/alg hydrogels, the water absorption of CTC/alg, ETC/alg, and TTC/alg was 93.8 ± 0.2%, 94.1 ± 0.2%, 94.2 ± 0.1%, respectively, and did not differ significantly (Fig. 4D). In contrast, the water absorption of the alginate control was significantly higher when compared with each of the NC/alg materials (97.6 ± 0.2%, $p < 0.05$). Swelling properties are important biological and mechanical considerations for the 3D bioprinting of anatomical constructs. Highly porous and hydrous biomaterials offer advantages as tissue emulators, supporting cell growth, nutrient diffusion, and migration. However, in the post-printing phase, excessive swelling can alter shape fidelity and structural integrity, adversely impacting the structural mimicry of the intended 3D construct (Dell et al., 2022). As such, the NC characterised in this study offers an advantageous balance of high porosity with significantly reduced swelling than that of alginate alone.

Overall, there were no striking differences in porosity, swelling, or water absorption among the NC/alg hydrogels, except for a significant difference in porosity between CTC/alg and TTC/alg. Among the materials tested, CTC/alg had the lowest porosity, swelling, and water absorption, whilst TTC/alg had the greatest, although the differences were typically marginal. The physicochemical data of NC hydrogel properties agree with our previous study using wood-pulp-derived NC, which had similar swelling and porosity percentages (Al-Sabah et al., 2019). Indeed, studies using hydrogels containing the structural analogue of cellulose, chitosan, also have similar swelling and water absorption properties. This suggests that NC and its analogues have comparable porosity and swelling properties irrespective of their biological source (Liu et al., 2018).

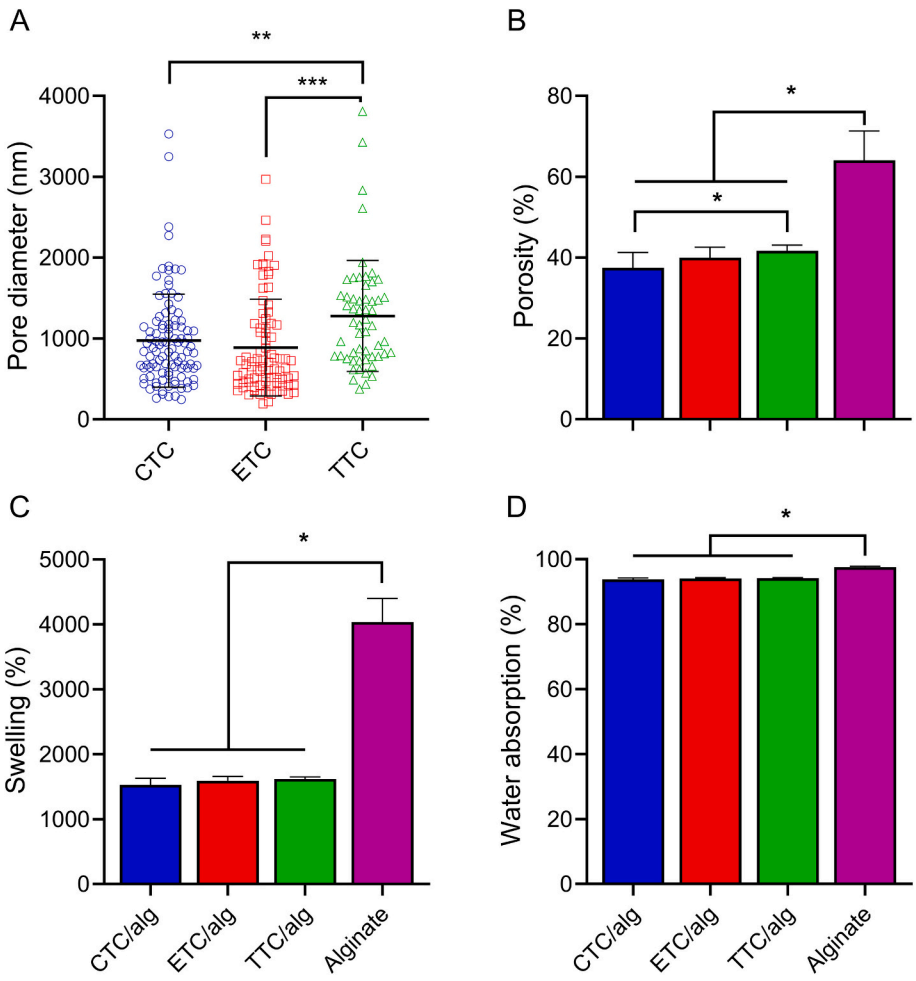

Fig. 4. Pore diameter of pure NC (A) and porosity, swelling, and water absorption of NC/alg hydrogels (B-D). Mean ± SD, $n = \geq 5$, * $p < 0.05$; ** $p < 0.01$; *** $p < 0.001$.

3.2. Raman spectroscopy

Cellulose has infrared- and Raman-active vibrational modes. Mean Raman spectra were similar between materials, with relatively little difference among the specific bond signatures (Fig. 5A). However, there were subtle changes in peak intensity between the 3 types of NC at 300–600 cm^{-1}, which are related to the skeletal bending modes involving C—C, C-O-C and O-C-C. There were also differences at 900–1200 cm^{-1}, and 1300–1450 cm^{-1}. Interestingly, the spectra of CTC and ETC were more similar to each other than they were to TTC. This is most clearly demonstrated by the principal component analysis (PCA) score plot (Fig. 5B) in which each repeat spectra are plotted as PCA1 against PCA4. CTC and ETC separate into distinct clusters primarily along the minor axis, with no overlapping spectra between the groups. TTC, on the other hand, had greater variability on both axes with no distinct clustering apparent. Indeed, numerous TTC spectra overlapped with CTC, although the general spectra of TTC were disparately spread, indicating greater material heterogeneity than for CTC and ETC.

The wavenumber ranges where peaks are observed in the spectra of NC correspond to specific bond signatures of cellulose. Such peaks, along with their corresponding chemical structure, are listed in Table 2. The low wavenumber region 250–600 cm^{-1} encompasses the peaks 330 cm^{-1}, 381 cm^{-1}, 432 cm^{-1}, 460 cm^{-1} and 514 cm^{-1}, corresponding to the skeletal bending modes C-C-C, C-O-C, O-C-C, and skeletal stretching modes C—C and C—O (Satha et al., 2020). The most intense peak, at 1097 cm^{-1} (cited in some literature as 1095 cm^{-1} or 1096 cm^{-1}), which was used to normalise the data, corresponds to C—H and C—H_2 stretching, as well as the asymmetric vibration of the C-O-C glycosidic linkage (Garavand et al., 2023). The wavenumber range of 1082–1170 cm^{-1}, corresponding to C-O-C and pyranose ring (skeletal) vibrations, contains the NC peaks at 1121 cm^{-1} and 1155 cm^{-1} (Mehanny et al., 2021). The recorded peak at 1235 cm^{-1} is within the documented range of 1232–1270 cm^{-1}. The peaks at 1377 cm^{-1} and 1479 cm^{-1} pertain to H-O-C and H-C-H bending respectively. Indeed, the FTIR spectra of each material also corroborates with the characteristic transmittance signature of pure NC structures (Supplementary Fig. 4 and Supplementary Table 1).

Raman spectroscopy demonstrated the unique signatures of NC corresponding to its distinct characteristic structures. Highly polar moieties such as water have weak Raman intensities due to relatively low polaris ability (Walrafen & Blatz, 1973). This makes Raman a superior vibrational spectroscopy for analysing biological materials with high water content, which otherwise interferes with other spectroscopies such as FTIR. Furthermore, cellulose is an optically heterogeneous material that can scatter light. However, refractive index variations are not detrimental to Raman due to the distance between excitation and absorption frequencies (Wiley & Atalla, 1987). There are subtle differences between the spectra of the three types of NC, which are also emphasised in the PCA analysis. Such differences are likely attributed to the extraction, processing, and chemical modification of each NC material, resulting in differential Raman spectra. The functionalisation of NC offers an array of opportunities to tailor the material for specific biomedical applications. The hydroxyl groups of NC are highly reactive and readily oxidised, generating negatively charged

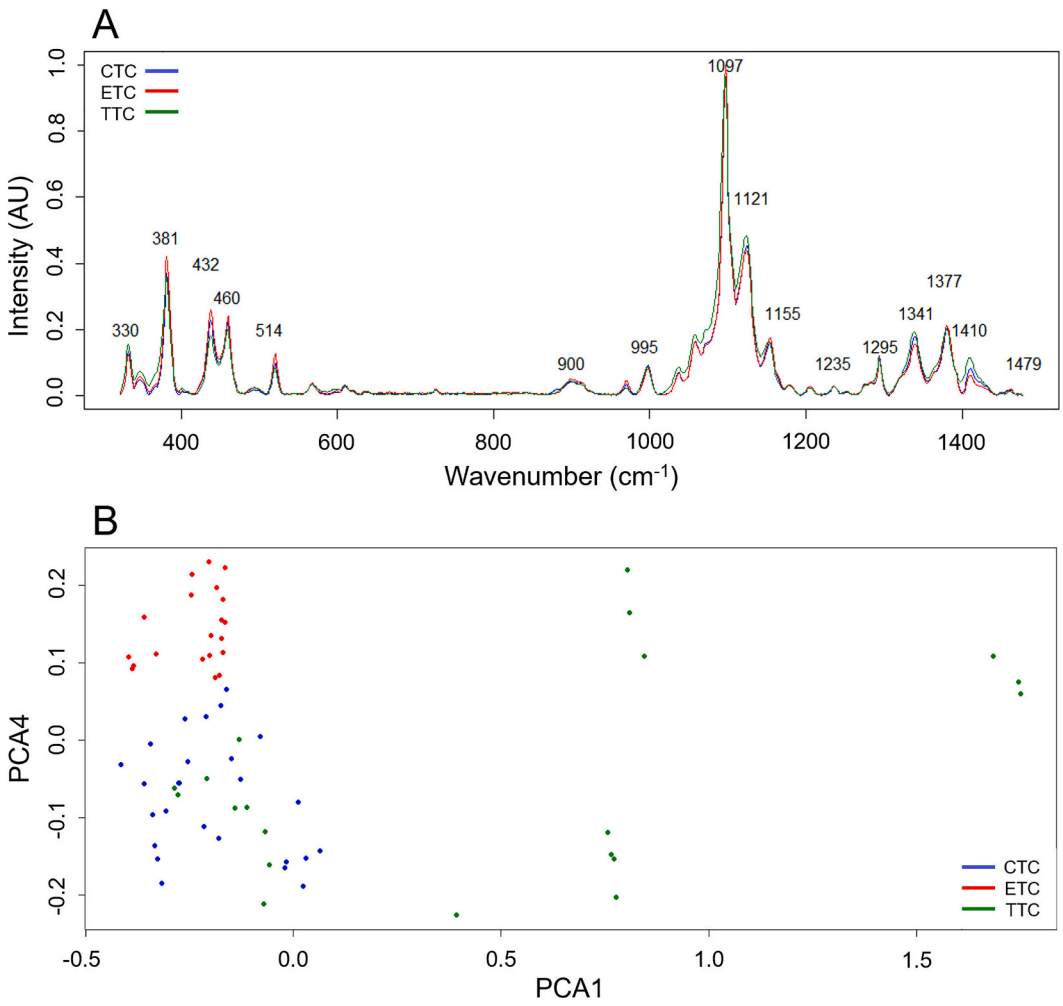

Fig. 5. Raman spectra (A) and PCA score plot (B) of pure CTC, ETC, and TTC.

Table 2
Raman peak assignments for NC structures.

Wavenumber (cm^{-1})	Structural Assignment
250–600	Skeletal bending modes C-C-C, C-O-C, O-C-C, and skeletal stretching modes of C—C, C-O
330	
381	
432	Within the 250–600 cm^{-1} region
460	
514	
1095/1097	C-H, C-H_2 stretching, asymmetric vibration of C-O-C glycosidic linkage
1082–1170	C-O-C, pyranose ring, skeletal, cellulose (fibre component)
1121	Within 1082–1170 cm^{-1} region
1155	
1235	Within 1232–1270 cm^{-1} range, C-O-C aryl-alkyl-ether
1377	H-O-C bending
1479	H-C-H bending

carboxylate (–COO^-) groups that support the incorporation of positively charged active molecules such as antimicrobial peptides (Weishaupt et al., 2018) and growth factors, which expedite wound healing (Picheth et al., 2014). Surface modifications also offer a platform for therapeutics, including controlled drug delivery. Moreover, functionalisation has relevance for scaffold engineering whereby hydrogel structure can be strengthened, stiffened, and toughened through polymer integration (Ghasemlou et al., 2021). Coincidentally, TEMPO oxidation does not affect crystallinity, as the reaction only occurs within the amorphous regions of the nanofibres (Saito et al., 2007) and so maintains the pertinent physicochemical properties of the material for tissue engineering.

3.3. Rheological properties

The storage modulus (G') represents the ability of a material to store energy elastically (i.e. the stiffness of the material). Conversely, the loss or viscous response modulus (G") is a measure of the energy dissipated through flow (i.e. the viscous response of the material). We first evaluated the G' and G" of each material at room temperature (22 °C). In each case, the storage modulus was higher than the loss modulus for all variants, indicating a dominance of elasticity in tunicate-derived NC (Fig. 6). This suggests a relatively strong interaction between individual fibrils within the overall structure and is supported by the nanostructure images reported earlier. These data align with previously published findings that have demonstrated elasticity in such systems, as reported for wood-derived NC (Dimic-Misic et al., 2018; Kyle et al., 2018). Interestingly, the storage and loss moduli of ETC were around an order of magnitude greater than those of CTC and TTC. Having a comparably high G' and G" is common in viscoelastic materials, which exhibit both solid- and liquid-like behaviour. High G' is typically associated with aligned polymer chains that store energy, and a high G" occurs when chains begin moving past each other as they dissipate energy, usually through heat.

Rheological characteristics of NC fibrils are highly dependent on

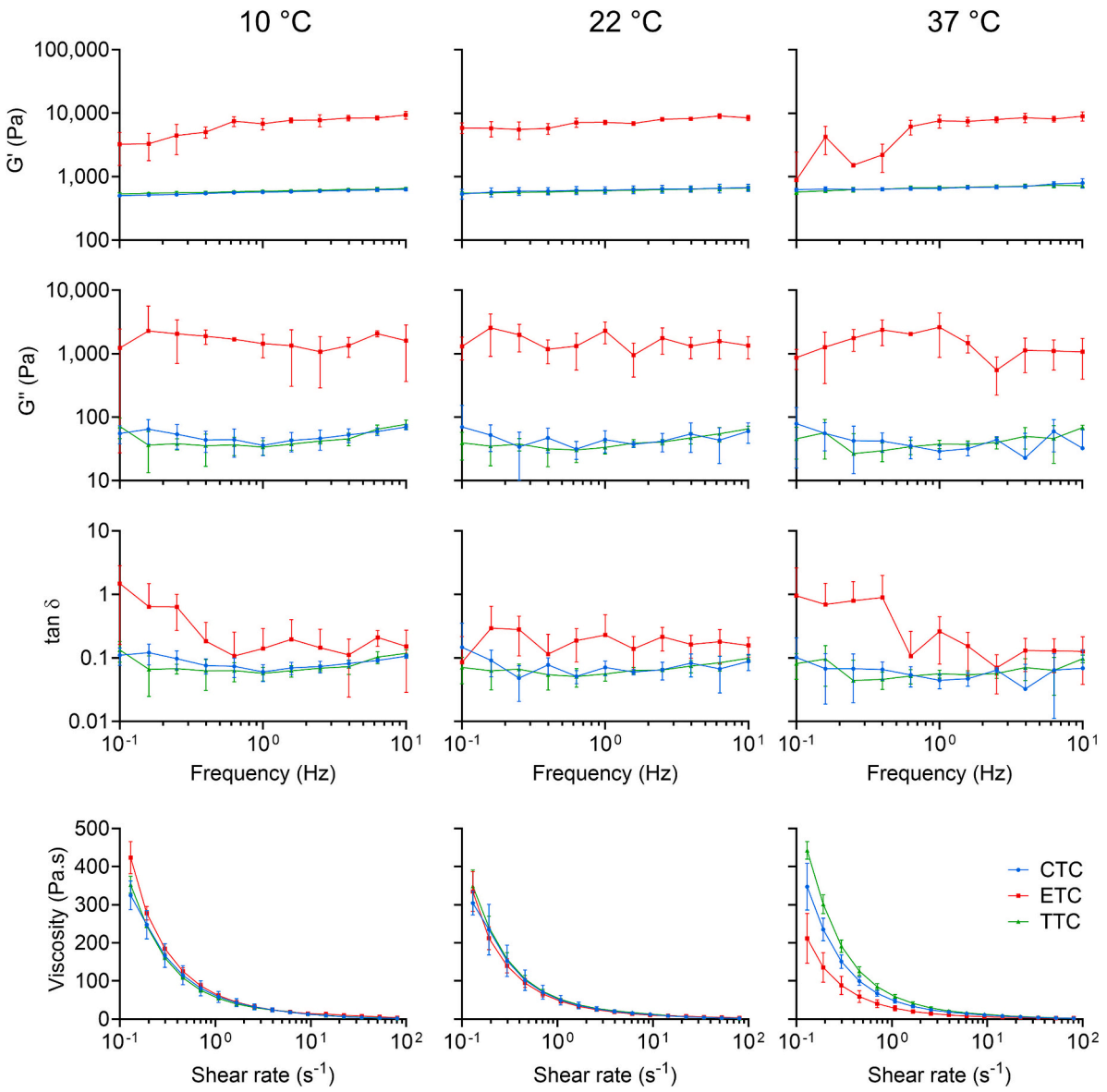

Fig. 6. Viscoelastic characterisation of pure NC. (Upper) Storage modulus (G'), (upper middle) loss modulus (G''), (lower middle) loss tangent (tan δ), and (lower) viscosity of CTC, ETC, and TTC at (left) 10 °C, (middle) 22 °C, (right) 37 °C. Mean ± SD, $n = 5$.

morphological properties such as length and diameter. Although the morphologies of each NC material were similar, ETC had the greatest length and width dimensions. Additionally, ETC exhibited a characteristic microstructure when imaged by cryo-SEM, with a high degree of entanglement and a large proportion of material existing either directly as a homogenous sheet or having a large quantity of interconnected fibrils between sheets. Such microarchitecture could create a more stable network structure with increased G' and G'' as observed in this study.

Temperature can also influence rheological characteristics of materials, including elasticity and viscosity (Moe et al., 1992). Many bioprinters can perform temperature-controlled extrusion of hydrogels, which can be used to regulate macromolecule assembly, as in the case of collagen, or improve cell viability by maintaining a physiologically relevant temperature during printing (Fan et al., 2016). We evaluated the rheology of NC at 10 °C, 22 °C, and 37 °C. The storage modulus of CTC and TTC was comparable across the different temperatures, and there was no significant difference between the means of the two materials at each temperature. However, the storage modulus of ETC was significantly higher than that of CTC and TTC at all temperatures ($p < 0.001$). Similarly, the loss modulus was comparable between CTC and TTC at each temperature. However, the loss modulus of ETC was significantly higher compared to CTC and TTC at each temperature ($p < 0.001$).

The loss tangent (tan δ) represents the ratio of the loss modulus to the storage modulus for viscoelastic materials. This parameter is a measure of the ratio of energy lost to energy stored during cyclic deformation and is given by the equation:

$$\tan\delta = G''/G'$$

When tan δ > 1, this indicates that the sample is dominated by viscous behaviour, whereas a tan δ < 1 indicates that the sample is dominated by elastic behaviour. The tan δ values for CTC and TTC were all <1 for each temperature tested, indicating that the material is dominated by elastic behaviour over the entire frequency range tested. There was no significant difference between the mean tan δ of CTC and TTC at any temperature, with both materials having very similar rheological characteristics. The loss tangent for ETC was also tan δ < 1 for the majority of measurements at each temperature. However, at lower frequencies, there were instances where the material was dominated by viscous behaviour, having a tan δ marginally >1, revealing a trend of

decreasing tan δ as frequency increased. This indicated that ETC viscoelastic behaviour is affected by the timescales of deformation, with longer timescales (i.e. smaller frequencies) producing a more viscous (liquid-like) response. Like the G' and G", the mean tan δ of ETC was significantly higher than that of CTC and TTC at each temperature ($p < 0.01$ for all). Some consider hydrogels with tan $\delta < 1$ to be weak gels, those with $0.1 < \tan \delta \leq 0.5$ as medium strength, and those with tan $\delta \leq 0.1$ indicative of strong gels (Pereira et al., 2022). This would categorise the pure NC used in this study as medium to high strength gels, making them appropriate candidates for anatomical 3D bioprinting where filament strength directly correlates to continuous filament extrusion and superior shape fidelity (Xu et al., 2019).

Shear rate ramps were used to evaluate the flow characteristics of CTC, ETC, and TTC by measuring viscosity as a function of shear rate at 10 °C, 22 °C, and 37 °C. All samples displayed robust non-Newtonian shear-thinning behaviour at each temperature, with viscosity decreasing as a function of shear rate (Fig. 6). Viscosity did not differ significantly between the NC materials at 10 °C and 22 °C. Indeed, viscosity was comparable between the two temperatures, indicating that ambient and lower temperatures do not have a significant impact on viscosity and the shear-thinning properties of NC. However, there were apparent differences in shear-thinning properties at 37 °C. Interestingly, at 37 °C, the TTC mean viscosity was shown to be higher than both the CTC and ETC across all shear rates. ETC demonstrated the lowest mean viscosity, which was significantly reduced when compared with TTC at 37 °C ($p < 0.023$). Although there was no significant difference between the mean viscosity of CTC and TTC at 37 °C, their shear-thinning profiles indicate that TTC possessed the highest viscosity, followed by CTC, and then ETC. The lower viscosity at this higher temperature indicates that ETC is thermally sensitive, and its rheological properties can be manipulated by adjusting the temperature. A lower viscosity at higher temperatures can facilitate easier shaping or moulding processes, making it suitable for applications that require flow or manipulation when heated. e.g. temperature-controlled extrusion. ETC has shown greater G' and G" than TTC and CTC and lower mean viscosity at 37 °C, indicating that while the material can store a significant amount of elastic energy (indicating stiffness), it can also dissipate energy more easily at elevated temperatures due to its lower viscosity. ETC exhibits a complex viscoelastic behaviour, where it can be "stiff" at high rates of deformation and lower temperatures but permits flow or deformation under lower rates of deformation and increased temperature.

Typically, higher viscosities result from particle-particle interactions initiated through hydrophobic interactions, hydrogen bonding, and electrostatic attraction. Conversely, electrostatic repulsion and solvation prevent aggregation by reducing interfibrillar interactions (Pääkkö et al., 2007; Xu & Li, 2018). Individually, such forces are weak, but collectively they amount to the formation of stable network structures that are disrupted under shear (Guvendiren et al., 2012). At low shear rates, NC structures are a coiled and highly interconnected mass. As shear is introduced, nanostructures untangle and align in parallel with the direction of flow. Increasing shear rate results in increasingly separated fibrils with markedly reduced viscosity, which is characteristic of non-Newtonian shear-thinning hydrogels (Wang, Sun, et al., 2018). This property makes NC hydrogels particularly pertinent for 3D bioprinting applications, particularly when bioink viscosity can be manipulated by print temperature. Typically, low temperatures increase viscosity, which enhances construct shape fidelity. However, the increased resistance of the bioink to flow results in additional force to move the material through the print nozzle. This results in cell deformation through shear stress which causes cell death and ultimately reduces viability of the construct (McCauley et al., 2025). Therefore, the ability to modulate the viscosity of the material to balance cell survival and shape fidelity, using a physiologically relevant temperature, is of significant advantage.

3.4. Printability assessment

NC is typically used in composite materials to enhance its printability and, more importantly, enable it to be crosslinked to maintain post-printing shape fidelity. In this study, 1% alginate was added to each NC variant to form NC/alg hydrogels. All hydrogels produced consistent and satisfactory print resolution as demonstrated by the straight-line assays (Fig. 7). Each material had clearly defined borders post-crosslinking, and a homogeneous internal structure occasionally punctuated by air bubbles unintentionally introduced during hydrogel preparation (Fig. 7A). As mentioned previously, alginate can be crosslinked with the divalent cation, Ca^{2+}, which binds the carboxyl group of guluronic moieties to form the conventional "egg-box" model. During the gelation reaction, alginate can shrink and contract, altering the final dimensions of hydrogel products (Kuo & Ma, 2008). Hydrogel line width was measured before and after crosslinking with $CaCl_2$ to determine the extent of shrinkage (Fig. 7B). In each case, mean line width was reduced between the native and crosslinked material with ETC having superior line width resolution in each case (986.7 ± 36.1 μm vs 869.6 ± 8.1 μm, $p = 0.005$), followed by TTC (1054.7 ± 4.5 μm vs 1007.2 ± 3.9 μm, $p \leq 0.001$), and finally CTC (1218 ± 37.1 μm vs 1185.3 ± 20.3 μm, $p = 0.247$). There was a significant difference in native CTC line width when compared with ETC and TTC ($p < 0.001$ and $p = 0.002$, respectively), and the line width of each crosslinked material also differed significantly between each of the respective materials ($p < 0.001$ for all). Interestingly, there was also a difference in the relative constriction of the line for each material, with ETC having the greatest percentage narrowing of mean line width (11.9 ± 0.8%), followed by TTC (4.5 ± 0.4%), and CTC (2.7 ± 1.7%). Whilst the shrinkage of alginate following ionic crosslinking is well characterised (Kuo & Ma, 2008), minimising shrinkage post-crosslinking is a desirable property for maintaining the construct macroarchitecture post-printing. The addition of carboxyl and carboxymethylated side groups in TTC and CTC, respectively, enable ionic bonding to occur not only within the alginate, but also between the NC fibrils and alginate, contributing to overall structural stability post-crosslinking (Lin et al., 2012). This in turn reduces the degree of shrinkage post-crosslinking meaning constructs more closely match the intended dimensions post-printing (Iudin et al., 2025).

3.5. Mechanical properties of NC/alg hydrogels

Each of the NC/alg hydrogels was compressed using uniaxial loading to evaluate mechanical deformation and strength. Each of the materials exhibited comparable strength characteristics up to approximately 50% compressive strain (Fig. 8A). Beyond this, CTC/alg presents a stiffer stress-strain response compared with ETC/alg and TTC/alg, which have almost identical stress-strain profiles. The ultimate compressive strength (UCS), strain, and Young's modulus were also recorded and compared between materials (Fig. 8B-D). The UCS between CTC/alg and ETC/alg was comparable and did not differ significantly (0.37 ± 0.08 vs 0.43 ± 0.03 MPa, respectively). Similarly, the UCS of CTC/alg and TTC/alg (0.25 ± 0.04 MPa) did not differ significantly. However, the UCS of TTC/alg was significantly lower than that of ETC/alg ($p < 0.05$). The ultimate strain (US; Fig. 8C) was comparable between CTC/alg (78.0 ± 0.0%) and TTC/alg (77.2 ± 0.0%), whilst the US of ETC/alg (83.3 ± 1.9%) was significantly higher than both CTC/alg and TTC/alg ($p < 0.05$ and $p < 0.01$, respectively). The Young's modulus was highest for ETC/alg, followed by CTC/alg, and lowest for TTC/alg (29.9 ± 0.9 kPa, 19.9 ± 7.8 kPa, and 13.7 ± 0.7 kPa, respectively). There was a significant difference between the Young's modulus of ETC/alg and TTC/alg ($p < 0.05$).

The compression testing indicates that ETC has the most robust mechanical properties of the three materials, whilst TTC is the weakest under uniaxial compressive load. These data corroborate the rheological findings, which demonstrate that ETC has a dynamic viscoelastic response of an order of magnitude greater than that of CTC and TTC.

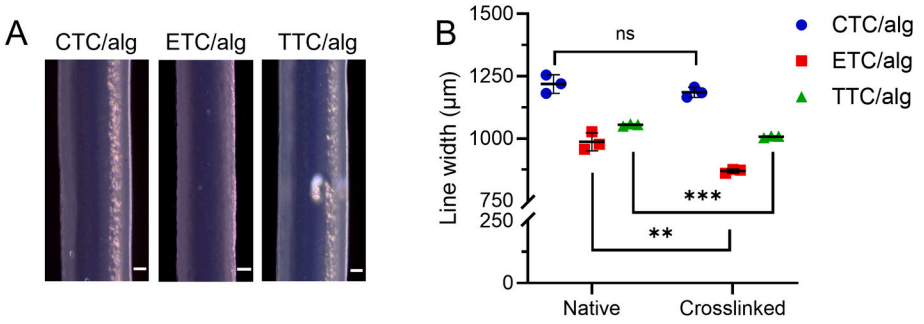

Fig. 7. Line resolution and effect of crosslinking on line width. (A) Representative images of line resolution for NC/alg hydrogels post-crosslinking. (B) Line width measurements of NC/alg hydrogels pre- (native) and post-crosslinking. Mean ± SD, $n = 9$, Scale bar = 200 µm, ** $p < 0.01$; *** $p < 0.001$, ns = not statistically significant.

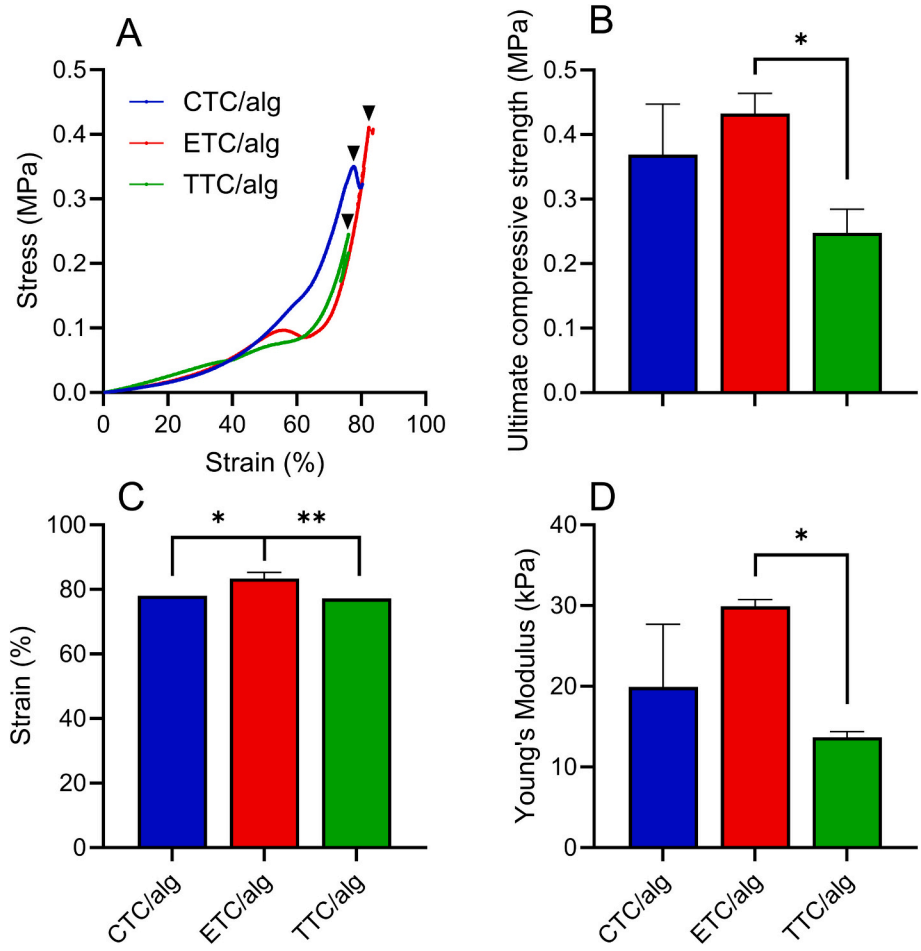

Fig. 8. Mechanical compression testing of NC/alg hydrogels. (A) Stress-strain curves of hydrogel under uniaxial compressive loading. Stress is plotted against strain, and black arrowheads represent the point of material failure. The average of 3 experiments is shown. (B) The ultimate compressive strength of the hydrogel. (C) The mean strain of the materials when compressed to the point of failure. (D) Young's modulus. Mean ± SD, $n = 3$, * $p < 0.05$, ** $p < 0.01$.

Furthermore, there is a correlation between the average pore size of materials, and mechanical strength, with ETC having the lowest mean pore size followed by CTC and TTC. This suggests increased interconnectivity between fibres that facilitates the transfer of stress from one fibre to another across a broad fibrillar network (Babaei-Ghazvini & Acharya, 2023).

Mechanical strength is an important consideration for the design and implementation of 3D bioprinted materials with real-world applications, particularly those that will be subject to some degree of load-bearing. For example, implantable medical devices (IMDs) for facial reconstruction, such as the ear, will need to have sufficient strength to retain their structure when implanted under the skin, as well as tolerance to external forces. Thus, ETC is a suitable candidate for further development in the design of tissue-engineered constructs.

3.6. Optical clarity

There was a clear difference in the optical clarity between each of the raw materials. When examined macroscopically, ETC was the most turbid of the NC suspensions, whilst TTC and CTC had optical

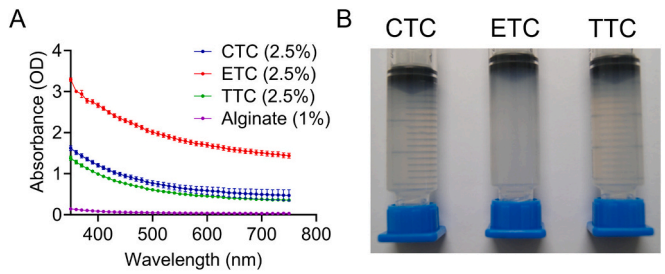

Fig. 9. Absorption spectra and optical clarity of pure NC. (A) Absorbance of CTC, ETC, and TTC was measured from 350 nm to 750 nm. 1% alginate is used as a reference. (B) Representative image of the optical clarity of NC. Mean ± SD, $n = 3$.

characteristics that were similar to each other (Fig. 9B). The absorbance of NC was quantified using a spectrum of wavelengths from near-UV (350 nm) to near-infrared (750 nm) with each material having a peak absorbance in the UV range (Fig. 9A). The maximum optical density (OD) of ETC was approximately double that of CTC and TTC at 350 nm (3.29 ± 0.04 OD vs 1.62 ± 0.06 OD and 1.38 ± 0.05 OD, respectively). In fact, there was a clear differentiation of ETC OD throughout the wavelength range, with the mean absorbance of ETC significantly greater than that of CTC and TTC (1.99 ± 0.49 OD vs 0.78 ± 0.32 OD and 0.62 ± 0.28 OD, respectively; $p < 0.001$). These data are consistent with the transparency of the materials when examined visually (Fig. 9B). Despite the similar absorbance spectra of CTC and TTC, there was a significant difference between the mean OD ($p < 0.001$), with the latter having the lowest OD and greatest optical clarity. The mean OD of 1% alginate, used as a reference, was significantly lower compared with CTC, ETC, or TTC (0.05 ± 0.02 OD; $p < 0.001$), which correlated with the optical clarity when examined macroscopically.

NC suspensions can exhibit flocs, particularly for mechanically and enzymatically treated material such as ETC. This results in opaque suspensions even at low NC concentrations (Karppinen et al., 2012). Transmittance of light is also wavelength-dependent and related to nanofibril width, with larger diameter fibrils scattering more light than narrower fibrils (Carr Jr. & Hermans, 1978). Accordingly, ETC had the highest mean OD, corresponding to the greatest mean width of any NC material in this study. In contrast, TTC had the narrowest mean width and the lowest mean OD. The oxidation of NC also increases transparency by creating a less polydisperse suspension. In fact, TEMPO-oxidation is the only method that can convert NC microfibrils into highly charged individual fibrils, decreasing light scattering and improving transparency (Isogai & Bergström, 2018). Such characteristics are important considerations for tissue engineering, where the optical clarity of 3D structures facilitates the examination of cells, materials, and their interaction. This is particularly beneficial for the visual evaluation of cellular activity using fluorescent markers to assess the interaction and behaviour of cells with materials within 3D constructs.

3.7. Biocompatibility

3.7.1. Cell viability within NC/alg hydrogels

The viability of human nasoseptal chondrocytes within NC/alg hydrogels of ETC, CTC, or TTC was evaluated at 24 h, 4 days, 7 days, 14 days, and 21 days using a LIVE/DEAD® viability assay (Fig. 10). As expected, the optical quality of captured images was superior in TTC/alg hydrogels, followed closely by CTC/alg. The least amount of transmitted light passed through ETC/alg hydrogels due to increased optical density. However, the fluorescence intensity was still satisfactory, and the images were of a suitable quality for the evaluation of cell viability (Fig. 10A). The ratio of live/dead cells remained consistent across materials, and there was no significant difference in cell viability between the hydrogels at any time during culture (Fig. 10B). There was also no significant difference in viability within hydrogels over time. Indeed, all materials demonstrated excellent cell viability with a mean of 75.5 ± 2.5%, 73.0 ± 3.9%, and 74.1 ± 3.9% for CTC/alg, ETC/alg, and TTC/alg, respectively, across the 21-day period. This suggests a stable turnover of cells and demonstrates the ability of the material to maintain cell viability in long-term culture for at least 21 days. This is an important attribute for tissue engineering where prolonged culture periods are commonly employed to facilitate enhanced mechanical strength of constructs through deposition of ECM (Jovic et al., 2025). We have previously demonstrated that the incorporation of cells into alginate only hydrogels resulted in a significant decrease in viability over 21 days (Jovic et al., 2023), unlike the viability in NC/alg hydrogels in this study, likely due to the NC fibres providing an anchor point for cell adhesion.

Scaffold material used in tissue engineering should, at least partially, mimic the dynamic functions of native ECM. The material architecture should provide a structure for cell attachment that facilitates new tissue formation and support biological and mechanical features, such as nutrient and metabolite transport, through an open porous structure (Chan & Leong, 2008). These data demonstrate that the NC used in this study provides the basic requirements for cell survival, and that viability is not influenced by surface modifications.

3.7.2. Immunogenicity of CTC, ETC, and TTC

The biocompatibility of NC was evaluated using a whole blood assay to assess the immunogenicity of each material. Blood was incubated with increasing concentrations of CTC, ETC, or TTC up to 1 mg/ml for 4 h or 24 h (Fig. 11). The presence of NC had no impact on the accumulation of the inflammatory markers IL-1β, IL-6, IL-8, or TNF-α for any of the materials tested, relative to the vehicle control. As expected, the positive control, LPS, stimulated a strong inflammatory response with significantly increased accumulation of IL-1β, IL-6, IL-8, and TNF-α compared with the vehicle control, ($p < 0.05$ for all; Fig. 9). Similarly, there was no difference in the accumulation of inflammatory markers between CTC, ETC, and TTC at any of the treatment concentrations nor was there an increased accumulation from 4 h to 24 h.

The biocompatibility of tunicate-derived NC is critical for use in translational medicine, particularly when considered as a component of an IMD. Biological contaminants such as bacterial LPS are primary initiators of inflammation, and LPS is the most common microbial mediator in sepsis and septic shock (Opal, 2010). Ensuring that NC is non-immunogenic, both natively and through the lack of microbial contamination, is critical for the clinical translation of tissue-engineered hydrogels used as IMDs. Immune cells are exquisitely sensitive to LPS, and humans are more susceptible to shock compared with other animals, requiring up to 10,000 times less LPS to induce sepsis (Chaiwut & Kasinrerk, 2022; Warren et al., 2010). Accordingly, the U.S. Food and Drug Administration has a strict limit of 20 endotoxin units (~ 10 ng LPS) per IMD product that directly or indirectly contacts the cardiovascular and lymphatic system (Food and Drug Administration, 2012). Using the whole blood model, we demonstrate that NC does not elicit an inflammatory response and indicates that the associated physicochemical properties of CTC, ETC, and TTC do not elicit inflammation, making these materials suitable candidates for clinical translation. To the best of our knowledge, this is the first study to investigate the cytokine response of whole blood when combined with NC, not only for tunicate-derived NC, but for any source of NC.

3.8. Biocompatibility in vivo

Materials that comprise IMDs must be tolerated by animals *in vivo*. Following the encouraging *in vitro* immunogenicity data, we tested the biocompatibility of NC composite constructs in C57BL/6 mice. Animals received 2 dorsal subcutaneous implants (Fig. 12A), which were explanted 14 days after implantation (Fig. 12B). No signs of clinical

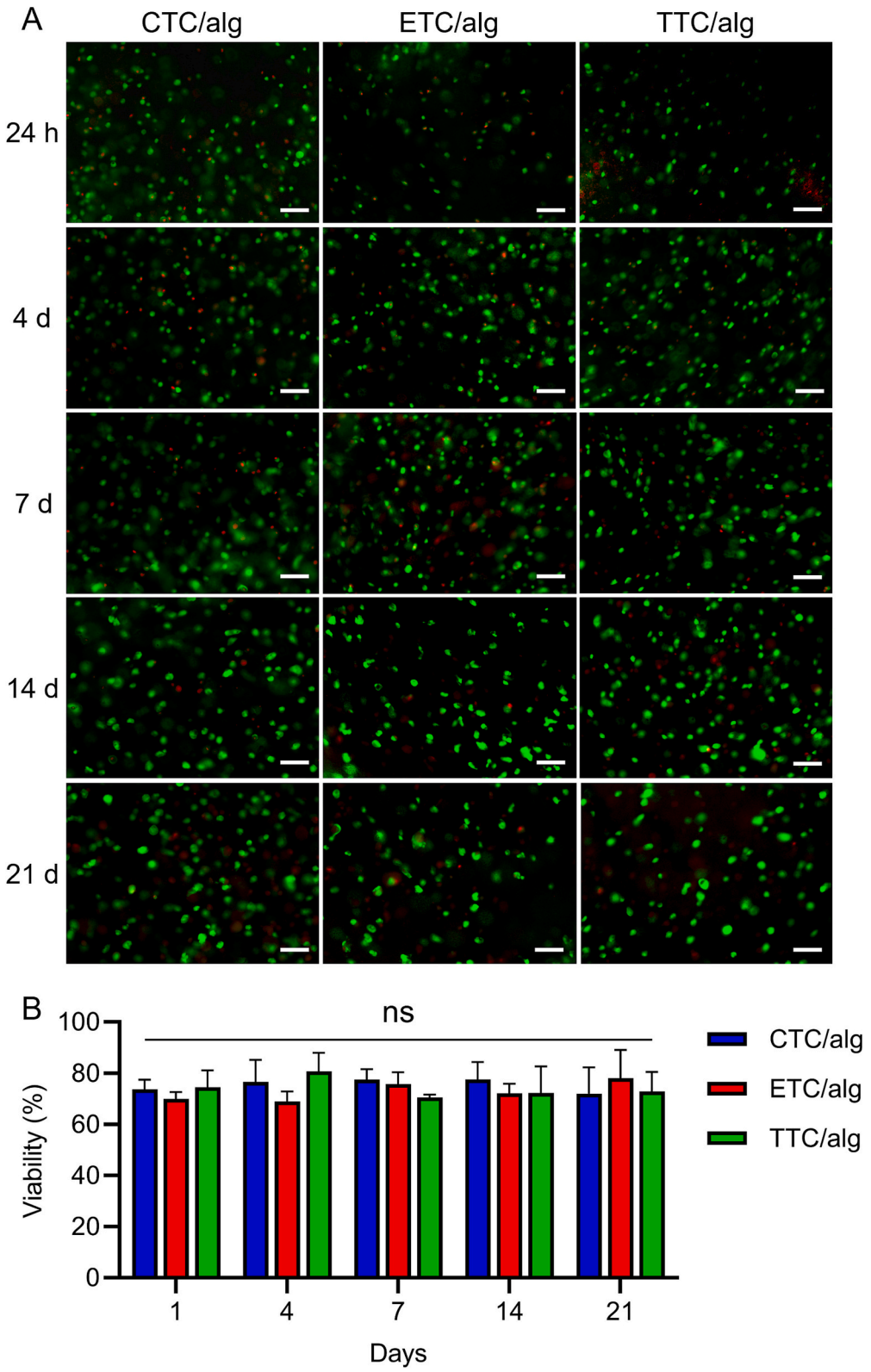

Fig. 10. Chondrocyte viability in NC/alg hydrogels after 24 h, 4 days, 7 days, 14 days, and 21 days in culture. (A) Live cells are stained with calcein-AM (green), and dead cells are stained with ethidium homodimer-1 (red). Images are representative of 3 independent experiments. Scale bar represents 100 μm. (B) Cell viability as a percentage of live cells to total cells for each corresponding material and day as determined from images. Mean ± SD, $n = 3$, ns = not statistically significant. (For interpretation of the references to colour in this figure legend, the reader is referred to the web version of this article.)

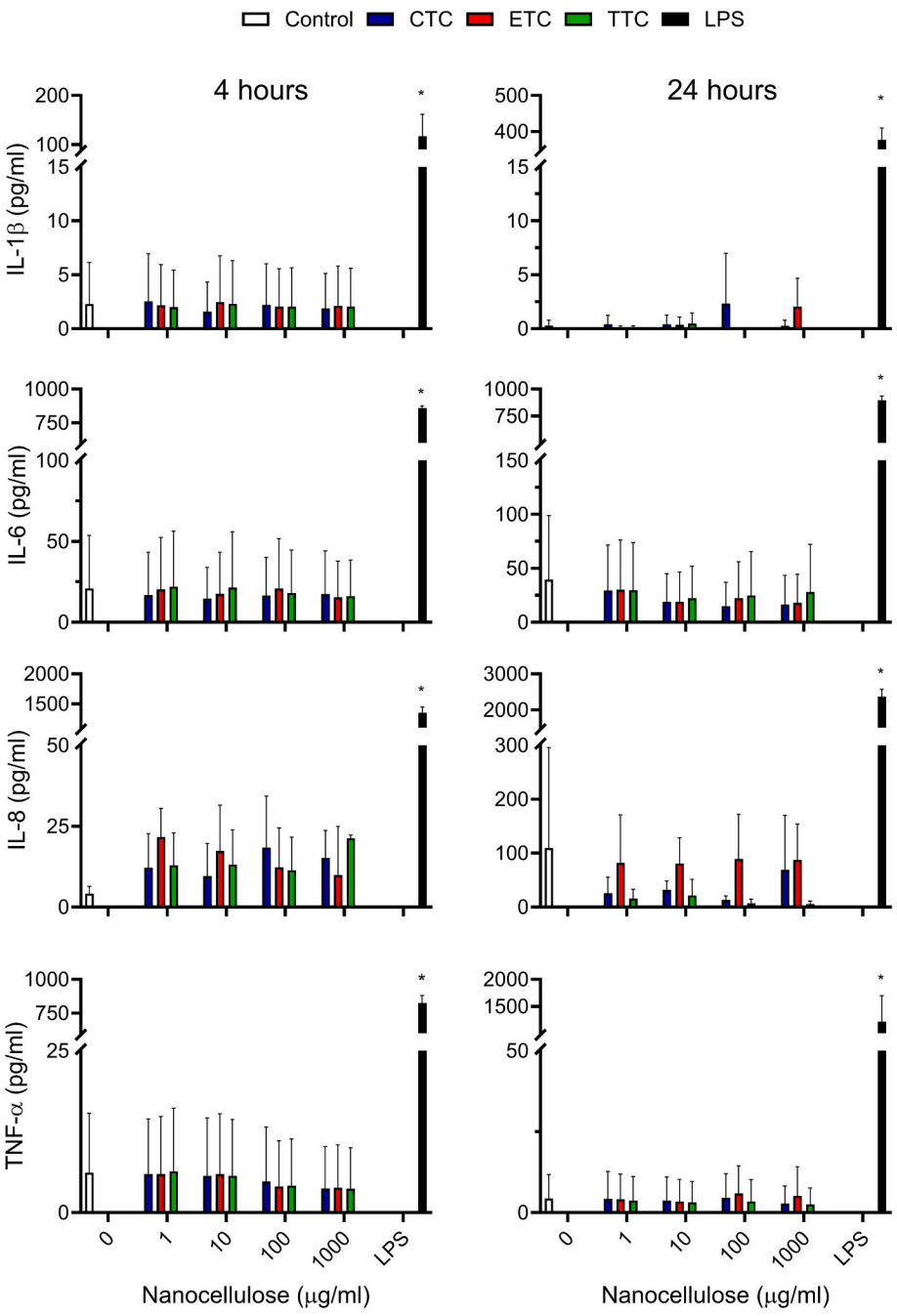

Fig. 11. Inflammatory response to pure NC. Whole blood was treated with vehicle control (white), or increasing concentrations of CTC (blue), ETC (red), TTC (green), or LPS (1 ng/ml; black) for 4 h (left) or 24 h (right). Mean ± SD, $n = 3$, * $p < 0.05$. (For interpretation of the references to colour in this figure legend, the reader is referred to the web version of this article.)

inflammation were observed during the postoperative evaluation 2 weeks after implantation. Healing was uneventful, and scaffolds maintained their structural integrity. Shape fidelity was well conserved, although some constructs migrated beneath the skin and approximately 10–20% of the total volume was reduced, likely through loss of water from the hydrogel (Fig. 12B). The major organs (heart, liver, and kidney) showed no abnormalities and were of a regular size, colouration, and appearance, with no evidence of disease or inflammation (Fig. 12C).

Explanted constructs were also sectioned and examined microscopically (Fig. 12D-G). Throughout the explant, moderate septal-like structures were present with sporadic and small areas of foreign body-type giant cell reactions with focal fibrosis (Fig. 12E and F). Although there was no evidence of neovascularisation within the biomaterials, blood vessels were present within the immediate proximity of the bioink (Fig. 12G) and there was evidence of connective tissue infiltration, suggesting biointegration of the material even at this early stage (Apelgren et al., 2022). However, most samples show a subcutaneous implant with occasional histiocytes in the periphery, encapsulated by a thin layer of fibrous tissue comprising a confluent lining of fibroblasts. The mean capsule thickness was 59.7 ± 15.8 μm, which is in line with the capsule thickness of IMDs made from commonly used materials such as titanium, polysulfone, and silicone (Bartoli et al., 2010). A prominent inflammatory and fibrotic area is present in the dermis of one animal, associated with focal epidermal ulceration, likely representing changes related to the implantation procedure. No animals were lost, and the mice remained healthy throughout the study.

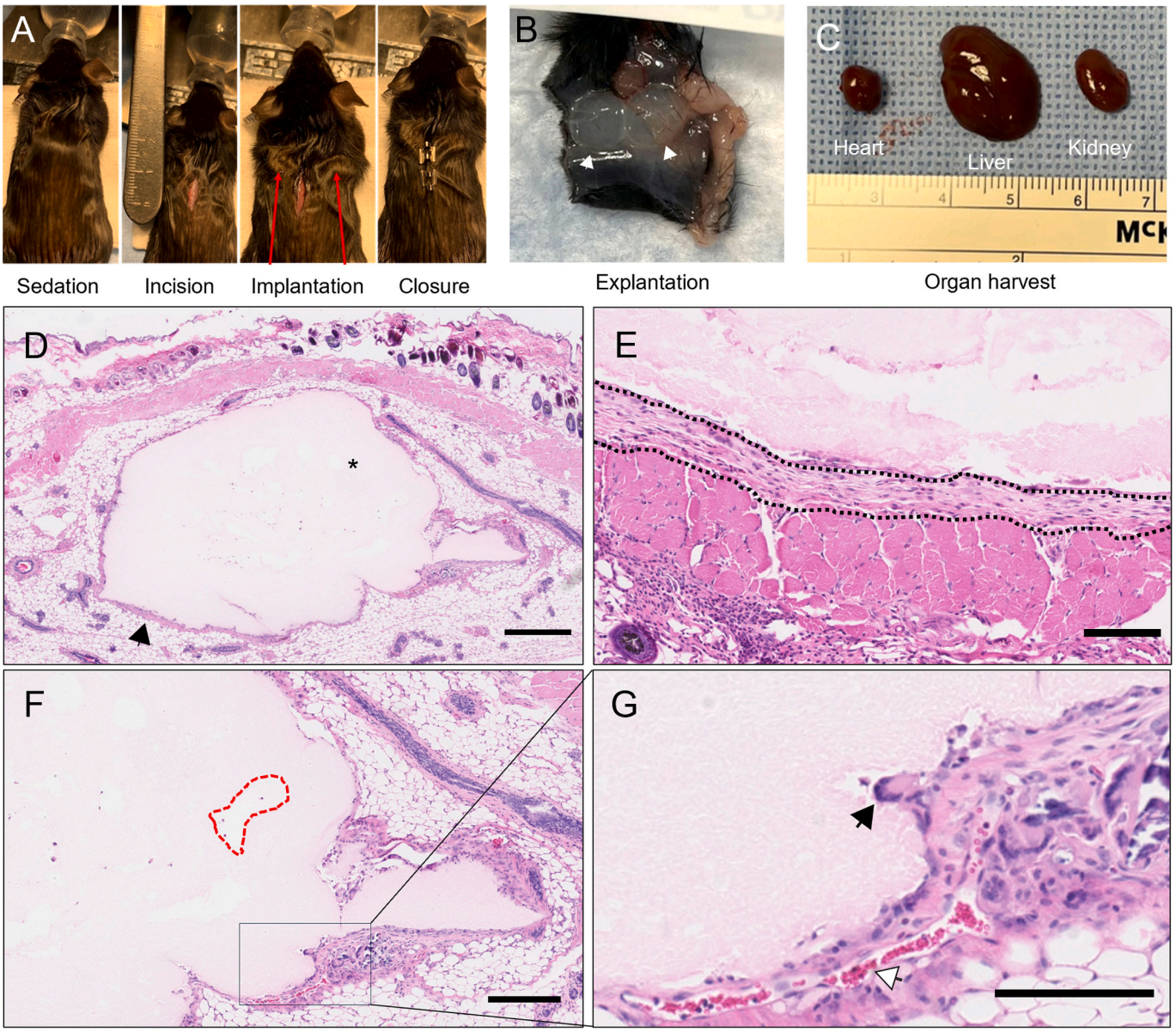

Fig. 12. Macroscopic and histological analysis of solid NC bioink implants after 14 days. (A) Bioink implantation procedure. (B) Explanted bioink constructs (white arrowheads point to individual constructs). (C) Macroscopic view of heart, liver, and kidney. (D) Sectioned biomaterial (asterisk) and fibrotic capsule (arrow). (E) Fibrotic capsule surrounding biomaterial (perforated lines) (F) Example of septal region within biomaterial (red perforated line). (G) Magnification of the boxed region in F showing a foreign body response giant cell (black arrow) and a blood vessel underlying the biomaterial (white arrow). Representative images shown. Scale bars 500 μm (D), 250 μm (E–F), 125 μm (G). (For interpretation of the references to colour in this figure legend, the reader is referred to the web version of this article.)

The inflammatory response to bioink constructs was evaluated *in vitro* and *in vivo* using a whole blood assay similar to that described in 3.7.2, and a mouse model, respectively. A crosslinked construct of 100 μl volume was submerged in 1 ml of whole blood for 24 h, and the inflammatory markers IL-1β, IL-6, IL-8, and TNF-α were quantified in culture supernatants. There was no significant accumulation of any markers relative to the untreated media control (Fig. 13A). However, there was an accumulation of IL-8 (media 18.1 ± 17.9 pg/ml vs bioink 525.9 ± 152.5 pg/ml, $p = 0.056$), although this was not statistically significant. LPS treatment resulted in significant accumulation of each inflammatory marker as anticipated. These results corroborate the NC whole blood data, which assessed the material in isolation, and demonstrate that as a composite, the bioink formulation has no adverse effect on the acute inflammatory response.

We also assessed the immune response of the animal to acellular bioink in a pilot study two weeks post-subcutaneous implantation. Blood samples collected from the animals were used in a proinflammatory multiplex array and compared with mice that received a skin allograft as a positive control stimulus. None of the inflammatory markers in the bioink group were significantly higher than allograft control (Fig. 13B). In fact, the cytokine profile of bioink-treated animals more closely resembled that of naïve animals lacking surgical intervention. Interestingly, MCP-1 and TNF-α were the most elevated markers in the bioink group, with the latter being a major regulator of inflammatory responses and the former a chemokine that recruits monocytes and macrophages to wound sites (Wood et al., 2014). We felt that it was important to use immunocompetent animals to assess the inflammatory and foreign body response to NC-based hydrogels, as nude animals are athymic and lack a fully functional immune system.

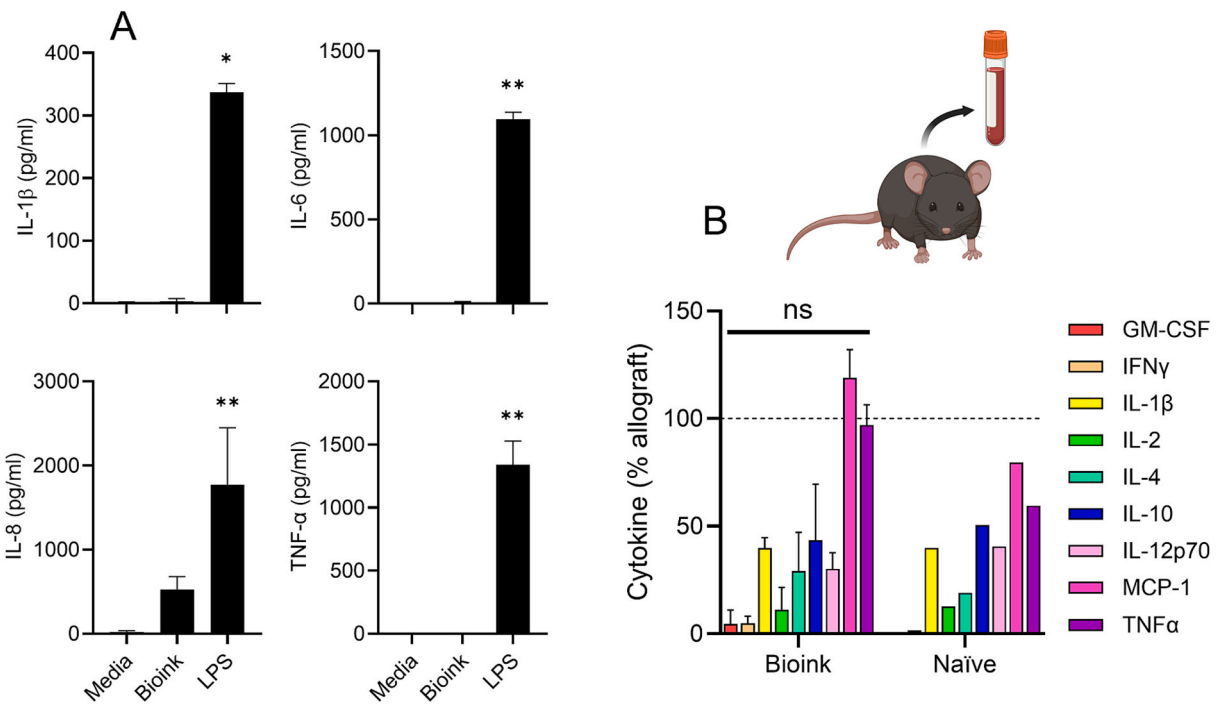

Fig. 13. Immunological response to bioink constructs. (A) Whole blood cytokine accumulation after 24 h incubation with vehicle control (media), bioink, or LPS (1 ng/ml). Mean ± SD, $n = 4$, * $p < 0.05$, ** $p < 0.01$. (B) Mouse cytokine profile 2 weeks post-implantation as a percentage of allograft control (dashed line) ± SD, $n = 5$, ns = not statistically significant.

4. Conclusions

Conventionally, NC used in tissue engineering have been derived from wood pulp or bacteria, with potential limitations including impurities, high processing costs, low crystallinity, and less favourable physicochemical properties. This study highlights the applicability of tunicate-derived NC for 3D bioprinting. Tunicates offer a sustainable alternative to traditional sources of NC, with high crystallinity and favourable mechanical properties for the development of tissue-engineered products used as IMDs.

We have demonstrated that each of the distinctly functionalised NC variants was a pure cellulose I structure with no evidence of contamination by exogenous polymers. Morphologically, each was comprised of a similar yet distinctive interconnecting mesh of fibrils with varying self-entanglement and porosity with ETC displaying a floc-like appearance. Mean fibril length and width measurements were relatively uniform with ETC having the greatest width and a correspondingly lower aspect ratio. Rheological evaluation revealed a dominance of elasticity in each of the variants, with ETC having greater storage moduli than CTC and TTC. In addition, an increase in temperature reduced the mean viscosity of ETC, suggesting that print temperature could be manipulated to influence printing parameters, and provide a beneficial environment for cell viability.

Ensuring the long-term material stability and viability of cells within such constructs is critical for creating viable tissue-engineered products for development of IMDs. We demonstrate that chondrocytes cultured for up to 21 days in tunicate-derived NC maintain a stable positive live/dead ratio for CTC, ETC, and TTC. The long-term culture of chondrocytes is necessary for the deposition of extracellular matrix, which we have recently demonstrated enhances the mechanical strength of constructs (Jovic et al., 2025) and enhances construct longevity, which is paramount where clinical translation is anticipated.

This study has highlighted the potential for tunicate-derived NC to be used as a prospective component of hydrogels for the formation of biomimetic tissue structures. We postulated that the different NC variants, CTC, ETC, and TTC, would have different physicochemical properties, including morphological, structural, mechanical, and rheological characteristics, which may have implications for 3D bioprinting suitability. Whilst some structural differences were demonstrated, each variant was well tolerated in mice, with stable structural integrity over 14 days. As such, the favourable mechanical properties, printability profile and biocompatibility of tunicate-derived NCs render them ideal base materials for composite bioinks, with tremendous potential for clinical translation.

CRediT authorship contribution statement

Matthew L. Turner: Writing – review & editing, Writing – original draft, Visualization, Project administration, Investigation, Formal analysis, Data curation, Conceptualization. **Thomas H. Jovic:** Writing – review & editing, Writing – original draft, Methodology, Conceptualization. **Lydia S. Bullock:** Writing – review & editing, Software, Methodology, Investigation, Formal analysis, Data curation. **Laurence Hill:** Methodology, Investigation, Data curation. **Bethan R. Thomas:** Writing – review & editing, Methodology, Investigation, Formal analysis, Data curation. **Salvatore A. Gazze:** Methodology, Investigation. **Thierry G. G. Maffeis:** Resources, Methodology, Investigation. **Lewis W. Francis:** Resources, Methodology. **Karl Hawkins:** Writing – review & editing, Resources, Methodology. **Yannick M. Sillmann:** Writing – review & editing, Methodology, Investigation, Formal analysis, Data curation. **Ana M.P. Baggio:** Writing – review & editing, Methodology, Investigation, Formal analysis, Data curation. **Peter R. Dunstan:** Writing – review & editing, Software, Resources, Methodology, Investigation, Formal analysis, Data curation. **Catherine A. Thornton:** Writing – review & editing, Resources, Methodology. **Fernando P.S. Guastaldi:** Writing – review & editing, Writing – original draft, Resources, Methodology. **Mark A. Randolph:** Writing – review & editing, Writing – original draft, Resources, Methodology, Investigation. **Iain S. Whitaker:** Writing – review & editing, Visualization, Supervision, Resources, Project administration, Methodology, Funding acquisition, Conceptualization.

Ethics approval

Human blood used in this study was obtained from healthy donors with informed consent and ethical approval was granted by Swansea University Research Ethics Committee (SUREC; 2022–0029, March 2022). Chondrocytes were isolated from waste surgical tissue obtained from patients undergoing routine rhinoplasty with informed consent and ethical approval from SUREC (IRAS 311495, May 2023). Animal experiments were approved by the Institutional Animal Care and Use Committee (2023N000138, August 2023) in compliance with the NIH guidelines for the care and use of laboratory animals.

Funding

This study was supported by The Scar Free Foundation & Health and Care Research Wales Programme of research in Reconstructive Surgery & Regenerative Medicine, which has been established in the ReconRegen Research Centre at Swansea University in partnership with Swansea Bay University Health Board. The funder had no role in study design, in the collection, analysis and interpretation of data, writing of the report, nor in the decision to submit the article for publication.

Declaration of competing interest

The authors declare that they have no known competing financial interests or personal relationships that could have appeared to influence the work reported in this paper.

Acknowledgements

The authors would like to acknowledge Ms. Kavitha Saw (Swansea Bay University Health Board) for providing nasal septum cartilage samples from which chondrocytes were isolated for use in this study, and Octavian Parkes for critical review of the manuscript. We would also like to thank Jonathan Widdowson for providing FTIR data.

Appendix A. Supplementary data

Supplementary data to this article can be found online at https://doi.org/10.1016/j.carbpol.2025.124671.

Data availability

The data generated in this study are available from the corresponding author on reasonable request. Data pertaining to patient and donor demographics are not made publicly available, in line with our ethical approval.

References

Abitbol, T., Rivkin, A., Cao, Y., Nevo, Y., Abraham, E., Ben-Shalom, T., Lapidot, S., & Shoseyov, O. (2016). Nanocellulose, a tiny fiber with huge applications. *Current Opinion in Biotechnology, 39*, 76–88. https://doi.org/10.1016/j.copbio.2016.01.002

Abu-Lail, N. I., & Camesano, T. A. (2003). Polysaccharide properties probed with atomic force microscopy. *Journal of Microscopy, 212*(Pt 3), 217–238. https://doi.org/10.1111/j.1365-2818.2003.01261.x

Al-Sabah, A., Burnell, S. E. A., Simoes, I. N., Jessop, Z., Badiei, N., Blain, E., & Whitaker, I. S. (2019). Structural and mechanical characterization of crosslinked and sterilised nanocellulose-based hydrogels for cartilage tissue engineering. *Carbohydrate Polymers, 212*, 242–251. https://doi.org/10.1016/j.carbpol.2019.02.057

Apelgren, P., Amoroso, M., Säljö, K., Montelius, M., Lindahl, A., Stridh Orrhult, L., … Kölby, L. (2021). Vascularization of tissue engineered cartilage - Sequential in vivo MRI display functional blood circulation. *Biomaterials, 276*, 121002. https://doi.org/10.1016/j.biomaterials.2021.121002

Apelgren, P., Samfors, S., Saljo, K., Molne, J., Gatenholm, P., Troedsson, C., … Kolby, L. (2022). Biomaterial and biocompatibility evaluation of tunicate nanocellulose for tissue engineering. *Biomaterials Advances, 137*, Article 212828. https://doi.org/10.1016/j.bioadv.2022.212828

Babaei-Ghazvini, A., & Acharya, B. (2023). The effects of aspect ratio of cellulose nanocrystals on the properties of all CNC films: Tunicate and wood CNCs. *Carbohydrate Polymer Technologies and Applications, 5*, 100311. https://doi.org/10.1016/j.carpta.2023.100311

Bartoli, C. R., Nadar, M. M., & Godleski, J. J. (2010). Capsule thickness correlates with vascular density and blood flow within foreign-body capsules surrounding surgically implanted subcutaneous devices. *Artificial Organs, 34*(10), 857–861. https://doi.org/10.1111/j.1525-1594.2010.01024.x

Benwood, C., Chrenek, J., Kirsch, R. L., Masri, N. Z., Richards, H., Teetzen, K., & Willerth, S. M. (2021). Natural biomaterials and their use as bioinks for printing tissues. *Bioengineering (Basel), 8*(2). https://doi.org/10.3390/bioengineering8020027

Brown, P. H., Balbo, A., Zhao, H., Ebel, C., & Schuck, P. (2011). Density contrast sedimentation velocity for the determination of protein partial-specific volumes. *PLoS One, 6*(10), Article e26221. https://doi.org/10.1371/journal.pone.0026221

Carr, M. E., Jr., & Hermans, J. (1978). Size and density of fibrin fibers from turbidity. *Macromolecules, 11*(1), 46–50. https://doi.org/10.1021/ma60061a009

Chaiwut, R., & Kasinrerk, W. (2022). Very low concentration of lipopolysaccharide can induce the production of various cytokines and chemokines in human primary monocytes. *BMC Research Notes, 15*(1), 42. https://doi.org/10.1186/s13104-022-05941-4

Chan, B. P., & Leong, K. W. (2008). Scaffolding in tissue engineering: general approaches and tissue-specific considerations. *European Spine Journal, 17*(Suppl 4), 467–479. https://doi.org/10.1007/s00586-008-0745-3

Coelho, C. C. S., Michelin, M., Cerqueira, M. A., Goncalves, C., Tonon, R. V., Pastrana, L. M., … Teixeira, J. A. (2018). Cellulose nanocrystals from grape pomace: Production, properties and cytotoxicity assessment. *Carbohydrate Polymers, 192*, 327–336. https://doi.org/10.1016/j.carbpol.2018.03.023

Dell, A. C., Wagner, G., Own, J., & Geibel, J. P. (2022). 3D bioprinting using hydrogels: cell inks and tissue engineering applications. *Pharmaceutics, 14*(12). https://doi.org/10.3390/pharmaceutics14122596

Dimic-Misic, K., Vanhatalo, K., Dahl, O., & Gane, P. (2018). Rheological properties comparison of aqueous dispersed Nanocellulose derived from a novel pathway-produced microcrystalline cellulose or by conventional methods. *Applied Rheology, 28*(6). https://doi.org/10.3933/applrheol-28-64474

Drury, J. L., & Mooney, D. J. (2003). Hydrogels for tissue engineering: Scaffold design variables and applications. *Biomaterials, 24*(24), 4337–4351. https://doi.org/10.1016/s0142-9612(03)00340-5

Dunlop, M. J., Acharya, B., & Bissessur, R. (2018). Isolation of nanocrystalline cellulose from tunicates. *Journal of Environmental Chemical Engineering, 6*(4), 4408–4412. https://doi.org/10.1016/j.jece.2018.06.056

Eichhorn, S. J., & Sampson, W. W. (2005). Statistical geometry of pores and statistics of porous nanofibrous assemblies. *J R Soc Interface, 2*(4), 309–318. https://doi.org/10.1098/rsif.2005.0039

Elazzouzi-Hafraoui, S., Nishiyama, Y., Putaux, J.-L., Heux, L., Dubreuil, F., & Rochas, C. (2008). The shape and size distribution of crystalline nanoparticles prepared by acid hydrolysis of native cellulose. *Biomacromolecules, 9*(1), 57–65. https://doi.org/10.1021/bm700769p

Fan, R., Piou, M., Darling, E., Cormier, D., Sun, J., & Wan, J. (2016). Bio-printing cell-laden Matrigel-agarose constructs. *Journal of Biomaterials Applications, 31*(5), 684–692. https://doi.org/10.1177/0885328216669238

Food and Drug Administration, U. S.. (2012). Guidance for Industry: Pyrogen and Endotoxins Testing: Questions and Answers. Retrieved January 28, 2025, from https://www.fda.gov/regulatory-information/search-fda-guidance-documents/guidance-industry-pyrogen-and-endotoxins-testing-questions-and-answers.

Garavand, F., Nooshkam, M., Khodaei, D., Yousefi, S., Cacciotti, I., & Ghasemlou, M. (2023). Recent advances in qualitative and quantitative characterization of nanocellulose-reinforced nanocomposites: A review. *Advances in Colloid and Interface Science, 318*, Article 102961. https://doi.org/10.1016/j.cis.2023.102961

Ghasemlou, M., Daver, F., Ivanova, E. P., Habibi, Y., & Adhikari, B. (2021). Surface modifications of nanocellulose: From synthesis to high-performance nanocomposites. *Progress in Polymer Science, 119*, Article 101418. https://doi.org/10.1016/j.progpolymsci.2021.101418

Gorroñogoitia, I., Urtaza, U., Zubiarrain-Laserna, A., Alonso-Varona, A., & Zaldua, A. M. (2022). A study of the printability of alginate-based bioinks by 3D bioprinting for articular cartilage tissue engineering. *Polymers (Basel), 14*(2). https://doi.org/10.3390/polym14020354

Gungor-Ozkerim, P. S., Inci, I., Zhang, Y. S., Khademhosseini, A., & Dokmeci, M. R. (2018). Bioinks for 3D bioprinting: An overview. *Biomaterials Science, 6*(5), 915–946. https://doi.org/10.1039/c7bm00765e

Guvendiren, M., Lu, H. D., & Burdick, J. A. (2012). Shear-thinning hydrogels for biomedical applications [https://doi.org/10.1039/C1SM06513K]. Soft Matter, 8(2), 260–272. doi:https://doi.org/10.1039/C1SM06513K.

Habibi, Y., Chanzy, H., & Vignon, M. R. (2006). TEMPO-mediated surface oxidation of cellulose whiskers. *Cellulose, 13*(6), 679–687. https://doi.org/10.1007/s10570-006-9075-y

Inoue, J., Nakashima, K., & Satoh, N. (2019). ORTHOSCOPE analysis reveals the presence of the cellulose synthase gene in all tunicate genomes but not in other animal genomes. *Genes (Basel), 10*(4). https://doi.org/10.3390/genes10040294

Isogai, A., & Bergström, L. (2018). Preparation of cellulose nanofibers using green and sustainable chemistry. *Current Opinion in Green and Sustainable Chemistry, 12*, 15–21. https://doi.org/10.1016/j.cogsc.2018.04.008

Iudin, D., Gerridzen, L. J. J. A., Bernal, N., Schuurmans, P., Neumann, C. C. L., Nguyen, M., van Steenbergen, L., Hak, M. J., Li, J., Casadidio, W., van Genderen, C., Masereeuw, A. M., Levato, R., van Ravensteijn, Y. S., B.G.P., & Vermonden, T. (2025). In-depth investigation of electrostatic interaction-based hydrogel shrinking for volumetric printing and tissue engineering applications. *Biomacromolecules, 26*(7), 4108–4123. https://doi.org/10.1021/acs.biomac.5c00117

Jessop, Z. M., Al-Sabah, A., Gao, N., Kyle, S., Thomas, B., Badiei, N., … Whitaker, I. S. (2019). Printability of pulp derived crystal, fibril and blend nanocellulose-alginate bioinks for extrusion 3D bioprinting. *Biofabrication, 11*(4), Article 045006. https://doi.org/10.1088/1758-5090/ab0631

Jovic, T. H., Gazze, A., Morgan, B., Hawkins, K., Francis, L., Arora, H., … Whitaker, I. S. (2025). Development of nanocellulose-hyaluronic acid bioinks for 3D bioprinting facial cartilages. *Carbohydrate Polymer Technologies and Applications, 11*, Article 100929. https://doi.org/10.1016/j.carpta.2025.100929

Jovic, T. H., Kungwengwe, G., Mills, A. C., & Whitaker, I. S. (2019). Plant-derived biomaterials: A review of 3D bioprinting and biomedical applications [review]. *Frontiers in Mechanical Engineering, 5*. https://doi.org/10.3389/fmech.2019.00019

Jovic, T. H., Nicholson, T., Arora, H., Nelson, K., Doak, S. H., & Whitaker, I. S. (2023). A comparative analysis of pulp-derived nanocelluloses for 3D bioprinting facial cartilages. *Carbohydrate Polymers, 321*, Article 121261. https://doi.org/10.1016/j.carbpol.2023.121261

Karppinen, A., Saarinen, T., Salmela, J., Laukkanen, A., Nuopponen, M., & Seppälä, J. (2012). Flocculation of microfibrillated cellulose in shear flow. *Cellulose, 19*(6), 1807–1819. https://doi.org/10.1007/s10570-012-9766-5

Kuo, C. K., & Ma, P. X. (2008). Maintaining dimensions and mechanical properties of ionically crosslinked alginate hydrogel scaffolds in vitro. *Journal of Biomedical Materials Research. Part A, 84*(4), 899–907. https://doi.org/10.1002/jbm.a.31375

Kwak, H. W., You, J., Lee, M. E., & Jin, H.-J. (2019). Prevention of cellulose nanofibril agglomeration during dehydration and enhancement of redispersibility by hydrophilic gelatin. *Cellulose, 26*(7), 4357–4369. https://doi.org/10.1007/s10570-019-02387-z

Kyle, S., Jessop, Z. M., Al-Sabah, A., Hawkins, K., Lewis, A., Maffeis, T., … Whitaker, I. S. (2018). Characterization of pulp derived nanocellulose hydrogels using AVAP® technology. *Carbohydrate Polymers, 198*, 270–280. https://doi.org/10.1016/j.carbpol.2018.06.091

Lam, E. H. Y., Yu, F., Zhu, S., & Wang, Z. (2023). 3D bioprinting for next-generation personalized medicine. *International Journal of Molecular Sciences, 24*(7). https://doi.org/10.3390/ijms24076357

Lin, L., Jiang, S., Yang, J., Qiu, J., Jiao, X., Yue, X., Ke, X., Yang, G., & Zhang, L. (2023). Application of 3D-bioprinted nanocellulose and cellulose derivative-based bio-inks in bone and cartilage tissue engineering. *Int J Bioprint, 9*(1), 637. https://doi.org/10.18063/ijb.v9i1.637

Liu, Q., Li, Q., Xu, S., Zheng, Q., & Cao, X. (2018). Preparation and Properties of 3D Printed Alginate–Chitosan Polyion Complex Hydrogels for Tissue Engineering. Polymers, 10(6), 664. doi:https://doi.org/10.3390/polym10060664.

Lin, N., Bruzzese, C., & Dufresne, A. (2012). TEMPO-oxidized nanocellulose participating as crosslinking aid for alginate-based sponges. *ACS Applied Materials & Interfaces, 4*(9), 4948–4959. https://doi.org/10.1021/am301325r

Marchessault, R. H., Morehead, F. F., & Walter, N. M. (1959). Liquid Crystal Systems from Fibrillar polysaccharides. *Nature, 184*(4686), 632–633. https://doi.org/10.1038/184632a0

Markiewicz, P., & Goh, M. C. (1994). Atomic force microscopy probe tip visualization and improvement of images using a simple deconvolution procedure. *Langmuir, 10*(1), 5–7. https://doi.org/10.1021/la00013a002

Markstedt, K., Mantas, A., Tournier, I., Martínez Ávila, H., Hägg, D., & Gatenholm, P. (2015). 3D Bioprinting Human Chondrocytes with Nanocellulose–Alginate Bioink for Cartilage Tissue Engineering Applications. Biomacromolecules, 16(5), 1489–1496. doi:https://doi.org/10.1021/acs.biomac.5b00188.

Martínez Ávila, H., Schwarz, S., Rotter, N., & Gatenholm, P. (2016). 3D bioprinting of human chondrocyte-laden nanocellulose hydrogels for patient-specific auricular cartilage regeneration. *Bioprinting, 1-2*, 22–35. https://doi.org/10.1016/j.bprint.2016.08.003

Martoïa, F., Perge, C., Dumont, P. J. J., Orgéas, L., Fardin, M. A., Manneville, S., & Belgacem, M. N. (2015). Heterogeneous flow kinematics of cellulose nanofibril suspensions under shear [https://doi.org/10.1039/C5SM00530B]. Soft Matter, 11(24), 4742–4755. doi:https://doi.org/10.1039/C5SM00530B.

McCauley, P. J., Fromen, C. A., & Bayles, A. V. (2025). Cell viability in extrusion bioprinting: the impact of process parameters, bioink rheology, and cell mechanics. *Rheologica Acta*. https://doi.org/10.1007/s00397-025-01504-z

Mehanny, S., Abu-El Magd, E. E., Ibrahim, M., Farag, M., Gil-San-Millan, R., Navarro, J., … El-Kashif, E. (2021). Extraction and characterization of nanocellulose from three types of palm residues. *Journal of Materials Research and Technology, 10*, 526–537. https://doi.org/10.1016/j.jmrt.2020.12.027

Moe, S. T., Draget, K. I., Skjåk-Bræk, G., & Simdsrød, O. (1992). Temperature dependence of the elastic modulus of alginate gels. *Carbohydrate Polymers, 19*(4), 279–284. https://doi.org/10.1016/0144-8617(92)90081-Z

Mukasheva, F., Adilova, L., Dyussenbinov, A., Yernaimanova, B., Abilev, M., & Akilbekova, D. (2024). Optimizing scaffold pore size for tissue engineering: insights across various tissue types [Review]. *Frontiers in Bioengineering and Biotechnology, 12*, 2024. https://doi.org/10.3389/fbioe.2024.1444986.

Nelson, M. T., Keith, J. P., Li, B.-B., Stocum, D. L., & Li, J. (2012). Electrospun composite polycaprolactone scaffolds for optimized tissue regeneration. *Proceedings of the Institution of Mechanical Engineers, Part N: Journal of Nanoengineering and Nanosystems, 226*(3), 111–121. https://doi.org/10.1177/1740349912450828

Nguyen, D., Hägg, D. A., Forsman, A., Ekholm, J., Nimkingratana, P., Brantsing, C., … Simonsson, S. (2017). Cartilage tissue engineering by the 3D bioprinting of iPS cells in a Nanocellulose/alginate bioink. *Scientific Reports, 7*(1), 658. https://doi.org/10.1038/s41598-017-00690-y

Opal, S. M. (2010). Endotoxins and other Sepsis triggers. In C. Ronco, P. Piccinni, & M. H. Rosner (Eds.), *Endotoxemia and endotoxin shock: Disease, diagnosis and therapy (Vol. 167, pp. 0)*. https://doi.org/10.1159/000315915. S.Karger AG.

Pääkkö, M., Ankerfors, M., Kosonen, H., Nykänen, A., Ahola, S., Österberg, M., … Lindström, T. (2007). Enzymatic hydrolysis combined with mechanical shearing and high-pressure homogenization for nanoscale cellulose fibrils and strong gels. *Biomacromolecules, 8*(6), 1934–1941. https://doi.org/10.1021/bm061215p

Percie du Sert, N., Hurst, V., Ahluwalia, A., Alam, S., Avey, M. T., Baker, M., … Würbel, H. (2020). The ARRIVE guidelines 2.0: Updated guidelines for reporting animal research. *BMC Veterinary Research, 16*(1), 242. https://doi.org/10.1186/s12917-020-02451-y

Pereira, K. A. B., Oliveira, P. F., Chaves, I., Pedroni, L. G., Oliveira, L. A., & Mansur, C. R. E. (2022). Rheological properties of nanocomposite hydrogels containing aluminum and zinc oxides with potential application for conformance control. *Colloid and Polymer Science, 300*(6), 609–624. https://doi.org/10.1007/s00396-022-04978-y

Picheth, G. F., Sierakowski, M. R., Woehl, M. A., Ono, L., Cofré, A. R., Vanin, L. P., … De Freitas, R. A. (2014). Lysozyme-triggered epidermal growth factor release from bacterial cellulose membranes controlled by smart nanostructured films. *Journal of Pharmaceutical Sciences, 103*(12), 3958–3965. https://doi.org/10.1002/jps.24205

Rahmani, S., Maroufkhani, M., Mohammadzadeh-Komuleh, S., & Khoubi-Arani, Z. (2022). Chapter 7 - polymer nanocomposites for biomedical applications. In A. Barhoum, J. Jeevanandam, & M. K. Danquah (Eds.), *Fundamentals of bionanomaterials* (pp. 175–215). Elsevier. https://doi.org/10.1016/B978-0-12-824147-9.00007-8.

Rojo, E., Peresin, M. S., Sampson, W. W., Hoeger, I. C., Vartiainen, J., Laine, J., & Rojas, O. J. (2015). Comprehensive elucidation of the effect of residual lignin on the physical, barrier, mechanical and surface properties of nanocellulose films[https://doi.org/10.1039/C4GC02398F]. Green Chemistry, 17(3), 1853–1866. doi:https://doi.org/10.1039/C4GC02398F.

Sacui, I. A., Nieuwendaal, R. C., Burnett, D. J., Stranick, S. J., Jorfi, M., Weder, C., … Gilman, J. W. (2014). Comparison of the properties of cellulose nanocrystals and cellulose Nanofibrils isolated from Bacteria, tunicate, and Wood processed using acid, enzymatic, mechanical, and oxidative methods. *ACS Applied Materials & Interfaces, 6*(9), 6127–6138. https://doi.org/10.1021/am500359f

Saito, T., Kimura, S., Nishiyama, Y., & Isogai, A. (2007). Cellulose Nanofibers Prepared by TEMPO-Mediated Oxidation of Native Cellulose. *Biomacromolecules, 8*(8), 2485–2491. https://doi.org/10.1021/bm0703970

Sapkota, J., Shirole, A., Foster, E. J., Martinez Garcia, J. C., Lattuada, M., & Weder, C. (2017). Polymer nanocomposites with nanorods having different length distributions. *Polymer, 110*, 284–291. https://doi.org/10.1016/j.polymer.2016.12.010

Satha, H., Kouadri, I., & Benachour, D. (2020). Thermal, structural and morphological studies of cellulose and cellulose nanofibers extracted from bitter watermelon of the Cucurbitaceae Family. *Journal of Polymers and the Environment, 28*(7), 1914–1920. https://doi.org/10.1007/s10924-020-01735-6

Sugiarto, S., Leow, Y., Tan, C. L., Wang, G., & Kai, D. (2022). How far is lignin from being a biomedical material? *Bioactive Materials, 8*, 71–94. https://doi.org/10.1016/j.bioactmat.2021.06.023

Sun, Y., Zhang, H., Li, Q., Vardhanabhuti, B., & Wan, C. (2022). High lignin-containing nanocelluloses prepared via TEMPO-mediated oxidation and polyethylenimine functionalization for antioxidant and antibacterial applications. *RSC Advances, 12*(46), 30030–30040. https://doi.org/10.1039/d2ra04152a

Thakur, V., Guleria, A., Kumar, S., Sharma, S., & Singh, K. (2021). Recent advances in nanocellulose processing, functionalization and applications: A review [https://doi.org/10.1039/D1MA00049G]. Materials Advances, 2(6), 1872–1895. doi:https://doi.org/10.1039/D1MA00049G.

Uppal, R. S., Sabbagh, W., Chana, J., & Gault, D. T. (2008). Donor-site morbidity after autologous costal cartilage harvest in ear reconstruction and approaches to reducing donor-site contour deformity. *Plastic and Reconstructive Surgery, 121*(6), 1949–1955. https://doi.org/10.1097/PRS.0b013e318170709e

Walrafen, G. E., & Blatz, L. A. (1973). Weak Raman bands from water. *The Journal of Chemical Physics, 59*(5), 2646–2650. https://doi.org/10.1063/1.1680382

Wang, D., Yu, H., Fan, X., Gu, J., Ye, S., Yao, J., & Ni, Q. (2018). High aspect ratio Carboxylated cellulose nanofibers cross-linked to robust aerogels for Superabsorption–flocculants: Paving way from nanoscale to macroscale. *ACS Applied Materials & Interfaces, 10*(24), 20755–20766. https://doi.org/10.1021/acsami.8b04211

Wang, H., Yu, H., Zhou, X., Zhang, J., Zhou, H., Hao, H., … Ma, D. (2022). An overview of extracellular matrix-based bioinks for 3D bioprinting [review]. *Frontiers in Bioengineering and Biotechnology, 10*. https://doi.org/10.3389/fbioe.2022.905438

Wang, Q., Sun, J., Yao, Q., Ji, C., Liu, J., & Zhu, Q. (2018). 3D printing with cellulose materials. *Cellulose, 25*(8), 4275–4301. https://doi.org/10.1007/s10570-018-1888-y

Warren, H. S., Fitting, C., Hoff, E., Adib-Conquy, M., Beasley-Topliffe, L., Tesini, B., … Cavaillon, J.-M. (2010). Resilience to bacterial infection: Difference between species could be due to proteins in serum. *The Journal of Infectious Diseases, 201*(2), 223–232. https://doi.org/10.1086/649557

Weishaupt, R., Heuberger, L., Siqueira, G., Gutt, B., Zimmermann, T., Maniura-Weber, K., … Faccio, G. (2018). Enhanced Antimicrobial Activity and Structural Transitions of a Nanofibrillated Cellulose–Nisin Biocomposite Suspension. *ACS Applied Materials & Interfaces, 10*(23), 20170–20181. https://doi.org/10.1021/acsami.8b04470

Wiley, J. H., & Atalla, R. H. (1987). Band assignments in the raman spectra of celluloses. *Carbohydrate Research, 160*, 113–129. https://doi.org/10.1016/0008-6215(87)80306-3

Wood, S., Jayaraman, V., Huelsmann, E. J., Bonish, B., Burgad, D., Sivaramakrishnan, G., … Shafikhani, S. H. (2014). Pro-inflammatory chemokine CCL2 (MCP-1) promotes healing in diabetic wounds by restoring the macrophage response. *PLoS One, 9*(3), Article e91574. https://doi.org/10.1371/journal.pone.0091574

Xu, C., Dai, G., & Hong, Y. (2019). Recent advances in high-strength and elastic hydrogels for 3D printing in biomedical applications. *Acta Biomaterialia, 95*, 50–59. https://doi.org/10.1016/j.actbio.2019.05.032

Xu, H.-N., & Li, Y.-H. (2018). Decoupling arrest origins in hydrogels of cellulose Nanofibrils. *ACS Omega, 3*(2), 1564–1571. https://doi.org/10.1021/acsomega.7b01905

Yu, W., Yi, Y., Wang, H., Yang, Y., Xing, C., Zeng, L., … Tan, Z. (2022). Effects of residual pectin composition and content on the properties of cellulose nanofibrils from ramie fibers. *Carbohydrate Polymers, 298*, Article 120112. https://doi.org/10.1016/j.carbpol.2022.120112

Zhao, Y., & Li, J. (2014). Excellent chemical and material cellulose from tunicates: Diversity in cellulose production yield and chemical and morphological structures from different tunicate species. *Cellulose, 21*(5), 3427–3441. https://doi.org/10.1007/s10570-014-0348-6